Article

Partial Oxidation of Methanol on MoO3 (010): A DFT and Microkinetic Study

Tej Choksi, and Jeffrey Greeley

ACS Catal., **Just Accepted Manuscript** • DOI: 10.1021/acscatal.6b01633 • Publication Date (Web): 09 Sep 2016

Partial Oxidation of Methanol on MoO_3 (010): A DFT and Microkinetic Study

Tej Choksi and Jeffrey Greeley*

School of Chemical Engineering

Purdue University

West Lafayette, IN 47907

*jgreeley@purdue.edu

Abstract

Methanol oxidation is employed as a probe reaction to evaluate catalytic properties of the (010) facets of molybdenum trioxide (MoO_3), a reducible oxide that exhibits a rich interplay of catalytic chemistry and structural transformations. The reaction mechanism is investigated with a combination of electronic structure calculations, using the BEEF-vdW and HSE06 functionals, and mean-field microkinetic modeling. Considered pathways include vacancy formation and oxidation, monomolecular dehydrogenation of methanol on reduced and non-reduced surfaces, bimolecular reactions between dehydrogenated intermediates, and precursor steps for hydrogen molybdenum bronze phase (H_yMoO_{3-x}) formation. Methanol dissociation begins with C-H or O-H scission, with the O-H route found to be kinetically and thermodynamically preferred. Dehydrogenation of CH_2O* to CHO* is slow compared to desorption, leading to complete selectivity towards CH_2O. C – H scission of CH_3O* and recombination of dissociated OH* to form H_2O* are kinetically significant steps exhibiting positive degrees of rate control, while oxidation of the reduced surface through adsorbed O_2 has a negative degree of rate control. The energetics of the latter elementary step are somewhat sensitive to the choice of density functional, and although this does not affect the predicted reaction orders, the overall rate may change. To estimate the impact of the surface oxidation state on the kinetics, the external pressure of oxygen is varied in the microkinetic model, and the reaction rate is found to follow a volcano-like dependency, with the optimum rate located where surface oxidation neither promotes nor inhibits the overall rate. The methodology demonstrated in this study should be more broadly applicable to modeling catalytic kinetics on reducible oxide single crystal surfaces.

Key Words: methanol oxidation, MoO_3, reducible oxide, DFT, microkinetic modeling

Introduction

Reducible oxides are extensively used as catalysts in the chemical industry for synthesis of bulk chemicals such as aldehydes[1–6], dimethyl ether[7], acrolein[8–11], acrylonitrile[12], and butadiene[13] because of their ability to selectively oxidize hydrocarbons. Most partial oxidation reactions on reducible oxides via a Mars van Krevelen mechanism[14] which entails oxidation of the hydrocarbon with concomitant reduction of the oxide surface through loss of a surface oxygen. Hence, these catalysts often display a complex relationship between surface structure and catalytic activity[15–21]. Molybdenum trioxide (MoO_3) is a particular reducible oxide that has seen application in partial oxidation reactions such as formaldehyde production from methanol[2,3,7,22–24], acrolein synthesis[8], alkene metathesis, hydrocracking[25,26], hydrodesulfurizaton,[27] and more recently, as a hydrodeoxygenation catalyst[28–31] for biomass to liquid fuel transformations. Single crystals[16–20,32,33], mixed metal oxides (iron and bismuth molybdates)[9,11,32,34–37], monomeric and cyclic trimeric clusters[38–40,41] (Mo_3O_9) on oxide supports, and polyoxomolybdate films[42,43] are among the many forms that this material may take. Further, in addition to its uses as a heterogeneous catalyst, MoO_3 has also been proposed as a hydrogen storage material[44] and as a possible host for Li intercalation in Li ion batteries[45].

The industrial application of MoO_3 as a catalyst for selective oxidation of alcohols, hydrocracking, and hydrodesulfurization motivated significant research in the 1980s[2,3,7,22,32]. The partial oxidation of methanol to formaldehyde, in particular, has served as a model chemistry to explore the relationship between the atomic-scale structure of the MoO_3 surface and its catalytic properties. Early experimental investigations confirmed that oxidation of methanol to formaldehyde and propylene to acrolein proceeds via a Mars van Krevelen mechanism[2,3]. Infrared experiments further suggested that methanol, water, and formaldehyde compete for the

same adsorption site[46], while Temperature Programmed Desorption studies indicated that the dehydrogenation step leading to formation of formaldehyde is the likely rate limiting step for the reaction[2]. Based on the inference that CH_2O desorption displayed first order kinetics, the activation energy and preexponential factor were evaluated as 20.6 kcal/mol and $2x10^{-7}$ s^{-1}, respectively. An additional infrared study suggests that formaldehyde and CO are produced at terminal oxygen vacancies while the bridged oxygen vacancy sites on high index crystal shear planes produce dimethyl ether and methyl formate[7]. The rate of formation of higher order products (dimethyl ether and methyl formate) decreases at high temperatures due to a reduction in concentration of the bridging oxygen vacancy as the shear planes are oxidized. Thus, higher order products are unlikely to be produced on (010) terraces present in the initial stages of methanol oxidation.

Experimental studies have generally concluded that lattice oxygen is the oxidizing species for methanol partial oxidation and that it is replenished by gas phase oxygen. However, even in the absence of gas phase oxygen, at a sufficiently high temperature, migration of oxygen atoms from the bulk to the surface ensures that the surface remains oxidized, thereby acting as a temporary buffer against surface reduction by methanol[47]. Bowker and coworkers demonstrated the importance of the highest Mo oxidation state in determining selectivity to formaldehyde by contrasting the rates and selectivity on MoO_3 (Mo in +VI state) and MoO_2 (Mo in +IV state) using TPD[48,49]. MoO_3 shows complete selectivity to the partial oxidation product, CH_2O, but when placed in anaerobic conditions, it shows a reduced selectivity to CH_2O. The Mo +VI atoms in MoO_3 under anaerobic conditions are reduced to the +IV oxidation state, possibly also leading to surface reconstruction, which is responsible for the shift in selectivity. Similar to anaerobic MoO_3, partial oxidation in anaerobic conditions over MoO_2, which can be thought of as a

limiting case of a reduced MoO_3 surface, leads to significant quantities of CO. In an environment with excess air, however, MoO_2 shows an increased selectivity to CH_2O.

Some recent studies on this system have focused on understanding the role of iron and molybdenum in iron molybdates using catalytic testing, XPS, EXAFS, XANES, and DFT calculations[34–37,50]. Iron molybdates are industrial catalysts for formaldehyde production from methanol. Chowdhry et al. showed that methanol oxidation on iron molybdate and MoO_3 involves loss of protons from surface methoxy species, and they concluded that the rate is higher on iron molybdate[32]. Brookes et al. studied MoO_x-modified Fe_2O_3 core-shell-type catalysts and concluded that a thin surface layer of MoO_x is essential to maintain selectivity to CH_2O[34]. If Fe is present at the surface, however, complete oxidation to CO is observed. Routray et al. independently investigated the Fe/Mo synergy and similarly deduced that the MoO_x layer at the surface is active towards formaldehyde formation[50]. Excess MoO_3 in the industrial catalysts (iron molybdate) replenishes MoO_x lost through volatilization on the surface.

As mentioned briefly above, there is a vigorous discussion in the literature about the crystallography of the active sites for methanol chemisorption and oxidation. Tatibouët and Germain proposed that the basal facets of MoO_3 are responsible for formaldehyde formation while higher order products such as dimethyl ether form on edge facets[23,24]. Atomic Force Microscopy (AFM) studies performed by Smith & Rohrer provided further evidence of the fact that undercoordinated Mo^{+6} cations on step edges or at defects are the active sites for the selective oxidation of alcohols[16,17,19,20]. Through TPD and gravimetric measurements, Farenth and coworkers deduced that methanol chemisorption coverages are consistent with an inactive (010) surface and localized adsorption on non - (010) planes[3]. Furthermore, the authors concluded that edge sites are responsible for the formation of all products. However, they

observed that, due to the possibility of reconstruction and the presence of surface defects, it would be difficult to deduce the exact nature of the active site with the methods they have applied. Additional evidence that coordinatively unsaturated Mo atoms are active for methanol chemisorption is provided by Chowdhry et al[32]. Through surface science UPS and TPD experiments, they concluded that no chemisorption was found on the (010) MoO_3 surface. However, powdered MoO_3 and ion-bombarded (010) surfaces of MoO_3 showed significant methanol chemisorption.

Smith and Rohrer characterized the evolution of the (010) surface in an atmosphere containing methanol and a varying ratio of oxygen and nitrogen[17]. They observed transformation of rectangular elongated pits to triangular pits that had an increased exposure of low coordinated atoms as the concentration of O_2 in the feed was reduced. These undercoordinated atoms are the hypothesized active sites. The active site debate is further complicated by restructuring of the catalytic surface to form hydrogen molybdenum bronze-like structures. Dissociative chemisorption of methanol on undercoordinated surface Mo's results in the formation of surface hydroxyl and surface methoxy groups. AFM studies by Smith and Rohrer exposing the (010) surface to nitrogen/alcohol (methanol, ethanol, or 2-propanol) mixtures indicate that MoO_3 can intercalate hydrogen to form acicular (needle-like) H_xMoO_3 precipitates[16,19]. Using formation of these precipitates as an indicator for methanol chemisorption, reactivity trends between mated pairs of the pristine and pitted (010) surfaces were compared. The pitted surfaces intercalated more hydrogen than the (010) surfaces, suggesting that these surfaces are more active for methanol partial oxidation. Further investigations pertaining to understanding the morphological changes of MoO_3 under reducing conditions showed that the (010) surface forms surface voids and has a high oxygen vacancy coverage[18,20]. This oxygen deficiency also led to the formation of

crystallographic shear planes, as alluded to above, which suggested that the surface vacancy coveragehad reached an upper limit. These planes were accompanied by formation of 2 Å high steps at the intersection of the planes and the (010) surface.

The above studies demonstrate that the (010) surface, which is the dominant facet of MoO_3, may reconstruct under reaction conditions, especially in more reducing environments. Although several experimental studies have shown this trend, relatively little is known about the molecular-level characteristics of the active surface and about how these characteristics evolve during catalytic processes. Desorption of water formed from methanol dehydrogenation will lead to formation of vacancies and undercoordinated adsorption sites, and as discussed above, these features may ultimately accumulate to form shear planes and other extended surface reconstructions. In the present contribution, we attempt to understand the relative competition between methanol oxidation and vacancy formation in the initial stage of reactivity where vacancy coverage isn't high enough to promote reconstructions. We also consider the competition between hydrogen intercalation, forming a bronze, and recombination, forming surface water and surface vacancies.

Motivated by the intriguing features of MoO_3 surface chemistry that have been revealed by the experiments described above, several theoretical studies have been undertaken to understand the physical and catalytic properties of the (010) surface of MoO_3. Chen et al. studied the crystal structure of MoO_3 using the LDA functional and Crystal Orbital Overlap Projection (COOP)[51] analysis. They concluded that all Mo – O bonds have a mixture of ionic and covalent character. The same authors also analyzed fundamental properties of MoO_3, such as binding energies of hydrogen, CH_3, and vacancy formation energies[52,53]. Coquet and Willock studied oxygen vacancy creation and O_2 adsorption on terminal oxygen defects on the (010) surface of

MoO_3 with the PBE + U functional[54]. Their analysis focused on the role played by the Hubbard model in localizing itinerant *d* orbitals. Their calculations showed that the terminal oxygen vacancy is energetically favorable in comparison with asymmetric and symmetric vacancies. Moreover, they observed that O_2 adsorbs as peroxy and superoxo anions on terminal oxygen defects.

A common observation of many DFT studies has been the inability of PBE, PBE+U, or LDA functionals to optimize the lattice vector along the [010] direction. The inability of these functionals to describe interactions occurring within the van der Waal's (vdW) gap is responsible for the large differences between experiments and theory in the [010] lattice vector. Ding et al., however, successfully modeled the MoO_3 (010) surface with van der Waals corrected density functionals[45,55]. Lattice constant optimization and vibrational frequency (Mo – O stretching) computation was performed with the DFT + D2[56] and vdw – DF[57] type functionals, yielding predictions within 1 and 5% of experimental values, respectively.

Several researchers have also studied the thermochemical and electronic properties of hydrogen in MoO_3. For example, Sha et al. examined hydrogen absorption and diffusion in bulk MoO_3 using DFT. Hydrogen absorption was found to result in a shift in the semiconductor band gap to metallic[44]. Adsorbed hydrogen was further observed to migrate within the lattice with a relatively small activation barrier of 0.13 eV. Hydrogen spillover, and an analysis of its subsequent diffusion on Pt/MoO_3, was studied by Chen et al. using the PW91 functional[58]. The authors reported diffusion barriers of 0.3 – 0.6 eV. The barrier for hydrogen hopping on the surface was calculated to be 0.51 eV. Migration of hydrogen into the bulk was found to have a barrier of 0.35 eV, and these DFT calculated activation energies are qualitatively similar to results of previous experimental investigations[59]. In addition to the thermodynamics of hydrogen

diffusion, Huang et al. reported anisotropic electronic properties in MoO_3 (010) by increasing strain and adsorbing hydrogen[60]. Electronic properties such as the density of states and band gap were found to be more strongly dependent on the strain along [001] as compared with [100] and [010] directions. A compressive (tensile) strain led to a smaller (larger) band gap and more (less) delocalized electrons along [001]. Modulating the electronic properties through electronic doping and adsorption of hydrogen resulted in similar trends for reducing the asymmetry along the [001] direction and for lowering the electronic band gap.

Finally, we turn to computational analyses of oxygenate chemistry on MoO_3(010). Pineiro and Lopez have recently analyzed activation of methanol on iron-doped MoO_3 surfaces. They concluded that the iron-doped catalyst exhibits increased activity compared to the undoped surface while maintaining high selectivity to formaldehyde[61]. Brookes et al. demonstrated, through DFT calculations and a multi-technique characterization study, that the presence of 1 ML of Mo oxide on iron oxide substrates is sufficient to maintain reactivity and selectivity to CH_2O[36]. Hence, the preferential surface segregation of Mo, existing in its highest oxidation state, governs selectivity to formaldehyde for the industrial catalyst. Mei et al. investigated the acetaldehyde HDO reaction network on the (010) surface on MoO_3[28]. The adsorption and reaction pathway for acetaldehyde HDO to ethylene on a terminal oxygen defect was studied, and DFT-calculated reaction barriers showed that dehydrogenation of acetaldehyde is kinetically and thermodynamically unfavorable in comparison with deoxygenation. A mechanism for terminal oxygen vacancy creation through formation of water through gas phase hydrogen adsorption, followed by water desorption, was also proposed. The Mo – O bond was described as being much stronger than the C – O bond, and thus, MoO_3 was able to remove O without C-C or C-H cleavage. The experimental and theoretical efforts described above highlight the need to

understand the atomic-level details of the relationship between MoO_3 surface structure and catalytic reactivity. As a first step towards this goal, the present investigation focuses on understanding the redox catalysis of MoO_3 at the molecular level during the early stages of surface reduction. Partial oxidation of methanol is employed as a probe reaction to obtain a molecular level understanding of the catalytic activity of (010) basal planes of MoO_3 and to estimate the likelihood of reconstruction under highly reducing conditions using first principles DFT calculations in conjunction with mean field microkinetic modeling, which is included to permit explicit determination of vacancy coverages as a function of reaction conditions. Kinetics and thermodynamics of an extensive reaction network comprised of monomolecular and bimolecular dehydrogenation pathways, hydrogen diffusion, surface reduction, and surface oxidation are calculated with BEEF-vdW and HSE06 functionals. Microkinetic modeling with the resulting free energy surfaces yields the preferred reaction pathway, apparent activation barriers, and reaction orders. The effect of oxygen pressure on turnover frequency and reaction mechanism is additionally studied in order to qualitatively estimate the role of oxygen vacancies in oxidation catalysis. Finally, the reaction kinetics are explained in terms of a simplified Langmuir-Hinshelwood model.

Computational Details

Electronic structure details: First principles periodic DFT calculations are performed with VASP5.3.3[62–64] using the Projector Augmented Wave (PAW) method[65–67]. Self-consistently calculated total energies are evaluated with the BEEF-vdW[68] and hybrid HSE06[69–71] functionals. Wellendorf et al. proposed the Bayesian Error Estimate Functional (BEEF-vdW) density functional[68]; which is constructed by applying principles of machine learning to obtain an

optimal fit with surface properties (binding energies), gas phase thermochemistry, and dispersion forces. The hybrid HSE06 functional partially corrects for self-interaction errors prevalent in standard GGA functionals. Hence, lattice constants and adsorption energies of reaction intermediates are calculated with HSE06 to validate findings with BEEF-vdW. All calculations are spin polarized unless otherwise stated. The electronic cores are represented by PAW PBE pseudopotentials. Lattice constants of α-MoO_3 are calculated with BEEF-vdW and HSE06 functionals by minimizing the stress on the unit cell at a kinetic energy cut off of 520 eV. Brillion zone integration is performed using (4,1,4) k-points generated with the Monkhorst-Pack scheme in reciprocal space[72]. Convergence of the calculations with respect to the k-point grid is confirmed. Partial occupancies are determined by a Fermi smearing of 0.1 eV ensuring rapid convergence of the Kohn-Sham equations.

α-MoO_3 crystallizes as an orthorhombic unit cell with a Pbmn space group. Top and side views of the oxide are shown in Figure 1. The structure consists of a series of bilayers with edge and corner-sharing octahedra oriented along the [010] direction which interact through weak van der Waals forces. The unit cell contains three crystallographically inequivalent oxygen atoms: the terminal oxygen, the bi-coordinated asymmetric oxygen, and the tri-coordinated symmetric oxygen (the latter species bonds with a Mo atom in the next sublayer). The van der Waals gap is surrounded with terminal oxygen atoms on either side. All bonds in MoO_3 have a significant degree of covalent character. The calculated lattice constants along the [100], [010] and [001] directions with BEEF-vdW and HSE06 are 3.70 Å, 15.21 Å, 4.06 Å, and 3.69 Å, 13.30 Å, 3.89 Å, respectively. The experimentally determined lattice constants for α-MoO_3 are 3.69, 13.86 and 3.96Å[73]. BEEF-vdW over estimates the lattice constant along [010], as the functional represents

a compromise between accurate vdW dispersion and surface thermochemistry, but this discrepancy is not expected to significantly impact surface energetics.

Adsorption and vacancy formation energies with BEEF-vdW are calculated on a series of supercells, including one- and two-bilayered (2x1x2, 2x2x2), as well as one-bilayered 3x1x3, 4x1x4 and 5x1x5, unit cells. The convention followed in naming the unit cell sizes is such that an Xx1xY unit cell represents X and Y number of octahedra along the [100] and [001] directions, respectively. The use of larger unit cells is necessary to minimize artefacts from periodic boundary conditions in adsorption/vacancy formation energetics due to long range electronic effects; this issue is discussed further in section 3.1. The bottom sublayer of the 2x2x2 two-bilayered slabs is fixed to simulate the bulk oxide. All atoms in the one-bilayered slabs for 2x1x2 to 5x1x5 supercells are relaxed. Adsorption energies on one-bilayered (2x1x2) and two-bilayered (2x2x2) slabs are nearly identical, with differences of less than 0.05 eV (see Supporting Information). Slabs are separated from their periodic images with 14 Å of vacuum. Dipole corrections are applied perpendicular to the slab (along [010]) to cancel spurious electrostatic interactions between images. Calculations are performed with a kinetic energy cutoff of 400 eV and (4, 1, 4) Monkhorst-Pack[72] k-point grid in reciprocal space, with adsorption energies converged to within 0.05 eV. The convergence limit of electronic energies for the Kohn-Sham equations is set to be 10^{-5} eV. Geometries are optimized until the magnitude of forces is less than 0.02 eV/ Å. Bader charges are further evaluated to understand trends in adsorbate binding on vacancies[74,75]. Transition state geometries are located using the Climbing Image Nudged Elastic Band (CI-NEB)[76,77] with eight total images, followed by refinement with the dimer method[78]. Two-bilayered 2x2x2 and one-bilayered 3x1x3 supercells are used for these kinetic calculations. Each transition state is checked for the presence of a single imaginary

frequency. The thermodynamic changes for elementary steps are calculated at infinite separation at the initial and final states, thus removing co-adsorbate effects, while activation barriers for these steps are reported as effective barriers from infinite separation. Further details about this approach are provided in section 3.1 of the results and discussion.

A two-step optimization scheme is employed for calculating adsorption energies with the HSE06 functional. Geometry relaxed calculations on 2x1x2 (one-bilayered slab with the bottom sublayer fixed) are performed at a kinetic energy cutoff of 300 eV and (2, 1, 2) Monkhorst-Pack k-points. The electronic and force convergence thresholds are set as 10^{-3} eV and -0.15 eV/ Å. The total energies differ by less than 0.01 eV when compared with electronic and force convergence thresholds of 10^{-4} eV and -0.10 eV/ Å, respectively. A spin polarized single point energy calculation is subsequently performed with an energy cut off of 400 eV and (4, 1, 4) k-points. Additionally, 3x1x3 one-bilayered calculations for selected adsorbates are performed to verify trends with BEEF-vdW. Vibrational frequencies, computed from the Hessian matrix under the harmonic approximation, are used to calculate zero point energy (ZPE) corrections. Graphics of molecular structures are created using the VESTA[79] program.

Gas phase energies are computed at a kinetic energy cutoff of 400 eV in 12 Å x 13 Å x 14 Å unit cells and with (1x1x1) k-points. Fermi smearing of 0.01 eV is employed. We note that the total energy of O_2 is overestimated with standard GGA functionals[80,81]. To account for this overbinding, the gas phase energy of O_2 calculated with BEEF-vdW and HSE06 is fit to the formation energy of H_2O (g) at 298.15 K. Such a scheme has been employed in electrochemical applications and is shown to mitigate the overbinding error[82,83]. Differences between corrected and DFT-computed gas phase energies for O_2 with BEEF-vdW and HSE06 are 0.64 eV and 0.01 eV, respectively. The DFT-calculated enthalpy change of methanol oxidation to formaldehyde in

the gas phase at 298.15 K and 1 bar differs from the experimental value by -0.26 eV and 0.17 eV with BEEF-vdW and HSE06, respectively. However, as the system under consideration for the kinetic model is far from equilibrium and at low conversion (approximately 5%), gas phase energies of other species are not adjusted to replicate the overall enthalpy change for methanol oxidation to formaldehyde in the gas phase; any differences in the thermodynamics are unlikely to affect the kinetic results. Equations used in calculating these corrections are included in the Supporting Information.

Entropy of Adsorbed species: Several studies have shown that adsorbed species may, in some cases, possess entropies significantly different than those calculated from vibrational frequencies within the harmonic approximation[84–87]. Sellers et al. report that entropies of molecular adsorbates on flat surfaces at low coverages can be accurately evaluated using the semi-empirical Campbell-Sellers equation[85,86]. This equation holds for desorption rates in the range of 0.001 to 100 monolayers per second. Thus, entropies of molecular adsorbates like CH_3OH*, CH_2O*, CO* and H_2O*, which have moderate-to-weak adsorption strengths on the (010) surface, are calculated using the Campbell Sellers approach (Equation 1). O_2*, in contrast, binds quite strongly in comparison with other molecular adsorbates for both functionals considered in this study, and the two lowest modes have relatively high frequencies of 186 and 171 cm^{-1}, respectively. The Campbell-Sellers equation is thus likely to overestimate the entropy of adsorbed O_2, and we compute the entropy using the simple harmonic approximation in this case. The Campbell -Sellers equation also cannot be directly applied to molecular fragments, as they often dissociate at temperatures lower than their desorption temperatures, and their entropies cannot be measured directly through surface science experiments. An alternative approach in these cases is to evaluate the fragments' entropy from a combination of harmonic vibrational

frequencies and two dimensional diffusion barriers[87]. In particular, we evaluate entropies of molecular fragments involved in methanol oxidation having their lowest modes > 150 cm^{-1} (CHOH*, OH* and O*) using the harmonic vibrational partition function. In contrast, CH_3O* and CHO* possess modes that are 109 cm^{-1}, 51 cm^{-1} and 113 cm^{-1}, respectively. Their entropies are calculated with a hindered translator partition function, which is based on the interpolation scheme for hindered translation developed by Terrell Hill[88]. A detailed derivation of the hindered translator scheme is presented in the Supporting Information. Entropies of all species are expressed in terms of J/mol K at 1 atm. throughout the manuscript.

$$S_0^{ad}(T) = 0.70 S_0^{gas}(T) - 3.3R \quad (1)$$

Microkinetic Model: The mean-field microkinetic model based on the pseudo-steady state hypothesis is formulated using methods developed in prior literature[89–96]. Rate constants for adsorption and desorption are modeled using collision theory. The area of a site is taken to be 10^{-19} m^2, and the sticking coefficient is assumed to be unity. Forward and reverse rate constants for surface reactions are calculated from classical transition state theory using ZPE-corrected kinetic and thermodynamic barriers evaluated at infinite separation, as determined by the BEEF-vdW and HSE06 potential energy surfaces. The individual rate constants are calculated such that the thermodynamic consistency of the gas phase reaction is maintained. The reaction network is modeled in a steady state CSTR operating under differential conditions (conversion between 4% – 6%) at 623 K and atmospheric pressure, consisting of a feed stream of 200 ml/s having a composition of 10% CH_3OH, 19% O_2, and balance N_2. The purpose of the reactor model is to ensure that kinetics are calculated at well-defined, experimentally-relevant gas phase partial pressures at steady state; the CSTR model is appropriate for this purpose. An additional benefit of employing such a reactor model is that selectivity between several serial pathways can be

computed without arbitrarily fixing partial pressures at the reactor outlet (see Supporting Information for additional details). Apparent activation energies are calculated between 623 and 625 K in increments of 0.5 K. Apparent reaction orders are evaluated by changing flow rates of one gas at a time in a range of ±20% of the standard inlet conditions (conversion varies from 4.09% to 5.9%). The N_2 flowrate is adjusted such that partial pressure of other gases remain unchanged. Campbell's degree of kinetic control[97,98] for a given transition state is evaluated by varying forward and reverse rate constants within a range of ± 5% such that the equilibrium constant and rate constants of the other steps remain unchanged. Simplified analytical expressions for the independent rates and coverages are determined the basis of the full numerical solution. Further details about model formulation, reactor size, steady state equations, and the LH expression are located in the Supporting Information.

Results and Discussion

Adsorption energies of reactive intermediates on MoO_3 (010)

Partial oxidation of methanol is generally thought to proceed via a Mars van – Krevelen mechanism, with oxygen vacancies present on the (010) surface functioning as the active sites[2–4,7]. Two primary decomposition routes, a pathway beginning with O – H scission and a pathway that commences with C – H bond breaking, have been postulated. Corresponding reaction intermediates are selected on the basis of previous experimental[2,3] and theoretical studies[91,99,100] for methanol oxidation. Dissociative chemisorption of methanol on an oxygen vacancy proceeds by either O – H scission to produce adsorbed CH_3O* (methoxy) or C - H scission to produce adsorbed CH_2OH* (hydroxymethyl). Subsequent H abstraction from methoxy by surface oxygen

atoms results in formaldehyde (CH_2O*), formyl (CHO*), and carbon monoxide (CO*) production. The hydroxymethyl pathway proceeds through cleavage of C – H bonds yielding hydroxymethylene (CHOH*) and hydroxymethylidyne (COH*), followed by O-H scission to yield carbon monoxide (CO*). The prospect of CH_2OH* and CHOH* undergoing O-H cleavage to produce CH_2O* and CHO* is also considered in a crossover pathway. Hydrogen atoms released in the reactions described above can either diffuse on the surface or towards the bulk, or they may combine with terminal oxygen atoms to form surface water. Hydrogen atoms adsorbed on lattice oxygen are termed as OH* species in this paper, unless otherwise stated. Subsequent desorption of water yields additional oxygen vacancies which help propagate the reaction. Conversely, surface oxidation proceeds through dissociative adsorption of gas phase oxygen on vacancies. Finally, in addition to pathways initiated by adsorption of methanol on oxygen vacancies, methanol oxidation pathways on the clean (010) surface, originating from weakly physisorbed methanol, are also evaluated. In our discussion of these pathways, we begin by considering the thermodynamics of vacancy formation and adsorption geometries of C_1 intermediates described above, followed by discussion of the free energy plots for both the methanol oxidation cycle and the MoO_3 redox cycle. Finally, we elucidate the most favorable reaction pathway and reaction kinetics through microkinetic modeling.

The thermodynamics of vacancy formation on asymmetric, terminal and symmetric oxygen atoms are calculated and presented in Table 1. Geometries of the vacancies are shown in Figure 2. Asymmetric and terminal oxygen vacancies possess the same geometries, and henceforth are referred to as the terminal oxygen vacancy. There is a slight geometric distortion for terminal oxygen vacancies with a Mo – terminal oxygen bond rotating upwards away from the surface. In addition to the rotation of the Mo – O bond, the Mo – asymmetric oxygen bonds

in the terminal oxygen defect have a significantly shortened bond length of 1.85 Å, as compared with 2.36 Å for the clean (010) surface. Unlike the terminal defects, symmetric oxygen vacancies show no geometry distortion. Vacancy formation energies are calculated on a series of supercell sizes ranging from 2x1x2 to 5x1x5 and are reported in Table 1 (see also notation in Figure 2). Interestingly, the terminal vacancy formation energy decreases by 0.83 eV as the supercell size is increased from 2x1x2 to 5x1x5 Mo octahedra units. This monotonic reduction in terminal oxygen defect formation thermodynamics seems to converge at the 5x1x5 supercell. In stark contrast, vacancy formation energies at the symmetric defect are independent of the unit cell size. Moreover, the symmetric defect is less stable as compared to the terminal oxygen vacancy by 2.13 eV. Finally, supercells containing 4 Mo octahedra along the [001] direction and 3, 4 and 5 Mo octahedra along [100] showed the same vacancy formation energetics. Hence, there is significant anisotropy in the effect of unit cell size on terminal vacancy formation energy, as extending the unit cell along [001] lowers energetics, while extending unit cells along [100] does not change the energies. This trend is confirmed with geometry optimized HSE06 calculations. The difference in terminal oxygen vacancy formation between 2x1x2 and 3x1x3 supercells is 0.69 eV, while the corresponding difference with BEEF-vdW is 0.48 eV. This correspondence, while not fully quantitative, suggests that the supercell size dependence of vacancy formation energy is a real physical effect and not simply the result of DFT errors.

Bader charge analysis is carried out to further understand this non-intuitive anisotropy (Table 1). The Bader charges calculated with BEEF-vdW on the 5x1x5 unit cell show that, surprisingly, the Mo atom with the vacancy has a Bader charge (3.59) close to that of an octahedrally coordinated Mo atom (3.69). Moreover, two Mo atoms adjacent to the vacancy (Mo – 1 and Mo – 2 in Figure 2) have significantly lower Bader charges of 3.38 and 3.30,

respectively. As is also shown in Table 1, trends in Bader charges of the five-coordinated Mo atom at the vacancy and the reduced Mo atoms behind it on 3x1x3 unit cells calculated with BEEF-vdW and HSE06 are similar. Thus, the electrons from the vacancy are specifically delocalized over two adjacent Mo atoms along the [001] direction. An increase in the number of octahedra along [001] leads to a more effective redistribution of charge on multiple Mo atoms, stabilizing the terminal oxygen defect. In addition to charge delocalization, the optimized vacancy configurations have distorted Mo – O (asymmetric) bonds. In fact, there is a contraction of 0.4 Å in the bond length, leading to compressive strain along the [001] direction. The distorted bond lengths for Mo – O bonds as a function of supercell size are given in the Supporting Information. An earlier study by Huang et al. demonstrated that strain along the [001] direction decreased the band gap of MoO_3[60], while strain effects along [100] and [010] had a negligible effect on the band gap.. Hence, the electronic structure in the [001] direction appears to be more sensitive to surface strain effects, and indeed the negative charge shifts from the vacancy to adjacent Mo atoms (Mo – 1 and Mo – 2 in Figure 2). An increase in the number of octahedra along [001], as in the (5x1x5) unit cell, creates more room to accommodate this geometric and electronic distortion, and the two reduced Mo atoms do not interact with their periodic images.

Adsorption geometries of C_1 intermediates in the methanol partial oxidation reaction network are calculated on the clean (010) surface (shown in the Supporting Information) and on terminal oxygen defects (adsorption on symmetric oxygen defects is not explicitly considered, as the formation energies of these vacancies is over two eV less favorable than that for the terminal vacancies). Geometries and binding energies of all adsorption configurations are shown in the Supporting Information. One-bilayered (2x1x2) and two-bilayered (2x2x2) supercells show very

similar adsorption energies. Hence, one bilayer is used for slabs with supercells larger than 2x1x2.

All C_1 adsorbates bind more strongly to the vacancies than to the clean (010) surface. The most stable adsorption geometries for C_1 intermediates are described below, with adsorption energies (calculated on the 4x1x4 supercell and referenced to the appropriate gas phase radicals) and Bader charges shown in Table 2, and adsorbate configurations shown in Figure 3. Negative adsorption energies denote exothermic binding. Additional adsorption configurations are illustrated in the Supporting Information. CH_3OH*, H_2O* and CH_3O* adsorb on the (010) surface through one Mo - O (in the adsorbate) bond. CH_3OH* adsorbs on the surface with a binding energy of -0.27 eV. CH_3O*, which has a geometry similar to CH_3OH*, binds with an adsorption energy of -2.14 eV. H_2O* is relatively weakly adsorbed, with a binding strength of 0.05 eV. CH_2O* and O_2* adsorb on the vacancy via two surface-adsorbate linkages (C – Mo, O – Mo for CH_2O* and two O – Mo bonds for O_2*) in a geometry termed button configuration, as shown in Figure 3. Adsorption energies of CH_2O* and O_2* are -0.48 eV and -1.88 eV, respectively. CHOH* and CO* bind through a single Mo – C bond and have adsorption strengths of -2.28 eV and -0.12 eV, respectively. We note, in passing, that in contrast to the state of the terminal oxygen vacancy with no adsorbates, the electronic charge is completely localized on the Mo atom to which the adsorbates bind (Table 2). Mo atoms adjacent to the adsorbate along the [001] direction therefore possess the same Bader charge as is observed on the unreduced surface (Figure 3 and Table 2), and no distortions in Mo – O bonds of the oxide along [001] for the species mentioned above are noted (Mo – O bond lengths along [001] adjacent to the adsorbate are shown in the Supporting Information).

CHO*, CH_2OH* and COH* adsorb on the terminal oxygen defect by forming linkages with not only the Mo atom at the vacancy, but also with an adjacent asymmetric oxygen atom, as shown in Figure 3. This geometry is termed the bridge configuration. CH_2O* also adsorbs in the bridge configuration, but it is not the most stable configuration, and hence is not discussed in detail. The bridge configuration induces a compression in the Mo – O (asymmetric) bonds (see Supporting Information) of the oxide near the adsorbate, akin to what is observed with the terminal oxygen defect. Bader charge analysis further confirms that there is charge delocalization along [001], with Mo atoms adjacent to the adsorbate (Mo -2 and Mo – 3 in Figure 3) being reduced (Bader charges are 3.3 – 3.4).

Analogous to what is observed for the terminal oxygen vacancy formation energies, a supercell size dependence is seen for adsorption energies of O_2*, H_2O*, and C_1 species that form bonds solely with the Mo atom at the vacancy. Similar to the oxygen vacancy formation energy, adsorption energies seem to converge at the 4x1x4 supercell size. Although these adsorption configurations do not show charge delocalization (Table 2 and Figure 3), the vacancy state to which adsorption energies are referenced exhibits this effect, and binding energies are therefore sensitive to the cell size. Correlations between binding energies on 4x1x4 supercells compared to 2x1x2 and 3x1x3 supercells are presented in Figure 4. The trend shows a straight line having a slope close to 1 and intercepts of 0.67 and 0.24 eV, respectively. Hence, adsorption energies of all C_1 species except bridge configurations of CH_2OH*, COH* and CHO*, have a near constant shift towards weaker binding as supercell sizes increase. However, the latter adsorbates, which are stabilized by a distortion in Mo – asymmetric oxygen bonds of the oxide, have binding energies invariant with supercell size. This is because the distorted Mo – asymmetric oxygen

bonds and delocalized charges on Mo's away from the adsorbate are present in both adsorbate and vacancy states, and hence any sensitivity to supercell size is removed.

While adsorption/desorption steps do show a unit cell size dependence, as described above, surface reaction thermodynamics are generally invariant with unit cell size, with the exception of a small number of elementary reactions that turn out to be kinetically irrelevant for the reaction network. These trends are further described in the Supporting Information. These considerations, together with results reported in Table 1, S9, and S10, demonstrate that unit cells with sizes of up to approximately (4x1x4) may be needed to remove spurious interactions between periodic images. We have emphasized this point, and the explanations for the observed behavior, in some detail to underline the importance of careful testing of finite size effects on the reducible oxide surfaces to obtain accurate thermodynamics and kinetics[101].

Prior DFT studies on metal oxide surfaces have suggested that adsorption energies of open shell molecular fragments like CH_3O* should be calculated in the presence of a coadsorbed H atom to ensure that Lewis acid/Lewis base type electron counting effects are correctly accounted for[102–106]. To evaluate the magnitude of this effect, we have checked adsorption energies and energy changes of other elementary steps in the presence of coadsorbed H. We observe that, on the reduced MoO_3 surface, the adsorbate is able to transfer charge to Mo ions, and an additional H atom far away from it is not required to accept the additional electron density. Thus, electron counting effects typically observed on irreducible oxides like La_2O_3 and MgO are not seen on adsorbates bound to oxygen vacancies of MoO_3. However, in contrast to the reduced surface, CH_3O* adsorbed on the clean surface, with no vacancies present, is unable to reduce Mo atoms and requires the presence of a coadsorbed H atom to balance the charge; hence, investigations of methanol oxidation on the clean surface should be performed in the

presence of appropriate numbers of coadsorbed H atoms. Further details pertaining to the energetics of methanol oxidation and the Bader charge analysis are presented in the Supporting Information.

Methanol oxidation and MoO_3 redox pathways

Transition state geometries involved in elementary reaction steps for methanol oxidation on MoO_3(010) are shown in Figure 5, while reaction kinetics and thermodynamics at 623 K for methanol oxidation and redox processes on the (010) surface of MoO_3 are given in the free energy diagram in Figures 6 and 7 (see Supporting Information for additional details). Entropies of adsorbates involved in the methanol oxidation pathway are listed in

Table 3. Entropies of gas phase species are calculated from the NIST Thermochemistry Webbook[107]. Methanol adsorption on terminal oxygen vacancies is endothermic, with a free energy change of 0.46 eV. Facile O – H scission to CH_3O* (activation barrier of 0.37 eV) is followed by C – H scission to yield CH_2O* with a barrier of 1.26 eV. Further C – H bond scission to CHO* has a barrier of 1.30 eV, while direct desorption of CH_2O* is exothermic (-0.18 eV). CHO* adsorbed in the bridge configuration binds to the surface through two C – O bonds, making the state extremely stable. As a result, removal of the fourth hydrogen forming CO* proceeds through a high energy transition state having a barrier of 2.11 eV. This barrier is split into a diffusional component, involving CHO* diffusion from the bridge to button configurations (1.55 eV), and an overbarrier of 0.56 eV to break the C – H bond. CO* desorbs relatively easily, with a barrier of -0.43 eV.

C – H scission of methanol through CH_2OH* is kinetically unfavorable compared to O – H scission, as the activation energy is 1.62 eV. This high effective barrier is partly a consequence

of the fact that methanol must be rotated to a metastable state, adsorbed through weak interactions between the CH_3 group and the vacancy, before C-H bond scission can occur. As shown in Figure 6, intermediates along the CH_2OH* pathway are thermodynamically unstable with respect to corresponding states along the CH_3O* route, and the kinetic barriers are also relatively high. Thus, methanol oxidation is very likely to proceed through initial CH_3O* formation. We note, however, that CH_2OH* and CHOH* dehydrogenation to form CH_2O* and CHO* have low barriers of 0.26 and 0.40 eV respectively, suggesting that these steps are quasi-equilibrated. Hence, CH_2OH* and CHOH* can form from intermediates along the CH_3O* route, but cannot further react due to unfavorable kinetics. These species are thus likely to exist as spectator species under typical reaction conditions. As shown below, these conclusions will be rigorously confirmed by the microkinetic model.

Diffusion barriers of CH_3O*, CH_2O*, and CHO* across the (010) surface are reported in Table 4. Although some of these barriers are relatively high (up to ~1.5 eV), they are nonetheless accessible at 623 K, justifying the use of mean-field microkinetic models and also suggesting the possibility of bimolecular collisions between these adsorbates. The most favorable bimolecular pathway has a net barrier for CH_2O* disproportionation to CH_3O* and CHO* of 0.64 eV. Other pathways involving different conformations of the two CH_2O* groups are comparatively less favorable and are described in the Supporting Information. Although this pathway could shift the selectivity towards CO by forming CHO*, the microkinetic analysis, described below, shows that bimolecular dehydrogenation is does not make a significant kinetic contribution due to low coverages of CH_2O*, CHO* and CH_3O*.

Finally, we note that, in comparison to the pathways on the reduced surface, methanol oxidation pathways on the unreduced (clean) surface have higher O – H and C – H cleavage

barriers, suggesting that rates on the unreduced surface will not be competitive with those on the reduced surface. This intuition is confirmed by comparing the respective rates with microkinetic modeling. These routes are described in more detail in the Supporting Information.

Surface hydroxyls formed from methanol partial oxidation can undergo transformations through three possible pathways: creation of H_2O*, intercalation of H* to form a hydrogen molybdenum bronze, and production of H_2. First, H*'s on adjacent terminal oxygen atoms can recombine to form H_2O* through an activated pathway having a low barrier of 0.10 eV. Subsequent desorption of H_2O* is highly exothermic at -0.64 eV, leading to the creation of terminal oxygen vacancies and reducing the surface. Dissociative adsorption of oxygen at the terminal oxygen defect site can then reoxidize the surface with a small overbarrier of 0.90 eV. Molecular oxygen adsorbs very weakly on the clean surface (binding energy of 0.3 eV). Thus, it is unlikely to play any role in terms of directly oxidizing methanol or oxidizing the reduced (010) surface. Hence, oxygen vacancies, which are active for methanol oxidation, are easily healed. The free energies of reactive intermediates in this redox pathway that occurs in tandem with methanol oxidation are shown in Figure 7. Second, H* adsorbed on a surface oxygen atom can diffuse across the (010) surface and into the bulk with relatively low barriers. The potential energy surface for hydrogen intercalation into the second layer is shown in Figure 8. These are prototypical precursor steps that will initiate the transformation of MoO_3 to a hydrogen molybdenum bronze. Despite barriers for hydrogen intercalation being less than 0.57 eV, and hydrogen diffusion between neighboring terminal oxygens having barriers of 0.46 eV, however, it is more likely that surface H*'s adsorbed on lattice oxygen atoms will recombine to form H_2O*, given the facile barrier for this elementary step and the highly exothermic desorption energy of H_2O*. Finally, the possibility of H* diffusion from O* to a vacancy, followed by

recombination with an additional H* to form H_2*, is studied. The activation barriers or diffusion of the first H* to an oxygen vacancy and formation of H – H bond are 1.76 eV and 0.65 eV respectively, and are thereby unlikely to compete with water formation. Experimental studies by Bowker and coworkers investigating methanol oxidation on MoO_3 report water formation and negligible hydrogen production under both aerobic and anaerobic conditions at 593 K[48], qualitatively confirming this conclusion of the DFT analysis. Thus, the kinetically most favorable route for H*'s will involve formation of H_2O* and its subsequent desorption to create an oxygen vacancy. The relative competition between molecular oxygen and methanol adsorption on the vacancies will determine the extent to which MoO_3 catalyzes methanol oxidation to formaldehyde compared to its own redox process.

As mentioned briefly in the previous section, the presence of coadsorbed hydrogen does not have a significant impact on adsorption energies on the reduced MoO_3(010) surfaces, while changes in unit cell size can have an impact on these adsorption processes. To investigate whether such effects impact barriers for key elementary steps, we perform additional calculations in the presence of a coadsorbed H* and on 3x1x3 supercells. The kinetics of key reactions (CH_3OH*, CH_3O* and CH_2O* dehydrogenation) are found to be largely invariant in the presence of an additional H atom, demonstrating that the due to its reducibility, MoO_3 is able to take up charge from the adsorbates bound to the terminal oxygen defects. In addition, barriers on the 3x1x3 and 2x1x2 supercells are generally within 0.1 eV, and hence artifacts arising from periodic boundary conditions do not affect the kinetic analysis. This result is expected as, in contrast to adsorption energies, the thermodynamics of most surface reactions are found to be largely invariant with unit cell size (see above), and transition state energies are often correlated

to surface reaction thermodynamics through the BEP principle[108]. Further details are given in the Supporting Information.

Free energies of methanol oxidation intermediates are also evaluated with the hybrid HSE06 functional to correct for spurious self-interaction errors arising from improper localization of *d* electrons. Reactive intermediates are relaxed on 2x1x2 unit cells with HSE06 lattice constants. Binding energies of all adsorbates, other than the bridge configurations of CHO*, CH_2OH* and COH*, are extrapolated to larger unit cell sizes through a constant shift of 0.69 eV towards weaker binding, as determined from the BEEF-VdW calculations. Adsorption energies of the bridge configurations of CHO*, CH_2OH* and COH* are invariant with unit cell size in BEEF-VdW and are therefore not corrected (see section 3.1). Figure 9 compares the thermodynamics of methanol oxidation and redox processes with BEEF-vdW and HSE06. There is a very close comparison for surface thermodynamics between the two functionals. Thus, conclusions related to the favorable CH_3O* pathway over CH_2OH*, and selectivity to CH_2O suggested by its favorable desorption free energy, are likely to be similar with both methods. However, there is one key difference between the two functionals. In contrast to BEEF-vdW, HSE06 binds O_2 on oxygen defects more weakly, by 0.69 eV. Thus, as we discuss further below, with the more accurate HSE06 functional, O_2 is predicted to be less likely to heal active sites, thereby enhancing the rate of methanol oxidation.

Microkinetic Modeling

Reaction rate constants and equilibrium constants for elementary steps are calculated from the DFT-determined energies. Elementary steps included in the microkinetic model are shown in

Table 5. These consist of the entire CH_3O* pathway, CH_3OH* dehydrogenation to CH_2OH* and its subsequent dehydrogenation to CH_2O*, bimolecular reaction of CH_2O*, and redox steps for the (010) surface of MoO_3. Pathways involving CHOH* and COH* are omitted, as these states are kinetically and thermodynamically unfavorable. This system contains four stoichiometrically independent rates which, for convenience, are taken to be r_1 (CH_3OH adsorption), r_5 (CH_2O* dehydrogenation), r_8 (CH_3OH* dehydrogenation to CH_2OH*, which is the first step of the CH_2OH pathway) and r_{10} (bimolecular dehydrogenation of CH_2O). Expressions relating rates of other elementary steps in terms of the independent rates are given in the Supporting Information. Turnover frequencies, coverages, apparent activation energies, and apparent reaction orders are shown in Table 6, while degrees of kinetic control are reported in the Supporting Information. The steady state kinetics in a CSTR are calculated at atmospheric pressure, a temperature of 623.15 K, and feed conditions of 10% CH_3OH, 19% O_2, and balance N_2 at a total flow rate of 200 ml/min; these are typical conditions for methanol oxidation in prior experimental studies[16,17].

Reaction pathways for methanol oxidation are shown in

Figure 10. The turnover frequency for formaldehyde formation computed with the BEEF-vdW energies is relatively low, at 1.15×10^{-4} s^{-1}. The apparent activation energy for CH_2O formation is 1.92 eV with apparent orders of CH_3OH and O_2 being 1.01 and -0.48, respectively (we note that it is useful to ensure differential conditions in the reactor for measurement of kinetic parameters, as oxygen pressure at the reactor outlet can influence the surface state - number of oxygen vacancies - and kinetics; hence, the temperature range used for the computation of the apparent activation energy is restricted to 623-625 K, and gas flow rates for apparent order calculations are changed within ±20% of the standard inlet conditions). Methanol

adsorption and its subsequent dissociation to CH_3O^* are quasi-equilibrated. C – H cleavage of CH_3O^* is kinetically significant, irreversible, and has a degree of kinetic control of 0.95. This irreversibility is a consequence of exothermic desorption of CH_2O^*, driving step 3 away from equilibrium. The near unity reaction order of methanol results from quasi-equilibrated dissociative chemisorption of CH_3OH to CH_3O^* and from the degree of kinetic control for C – H scission of CH_3O^* being 0.95. Thus, the overall rate will be directly proportional to methanol pressure. Low CH_2O^* coverage, coupled with a C – H scission barrier to form CHO* of 1.30 eV, leads to the rate of CHO* formation being $1.4x10^5$ times smaller in comparison with CH_2O^* desorption, thus maintaining selectivity to the partial oxidation product. As a consequence of very low CH_2O^* coverage ($1.97x10^{-12}$), the direction of bimolecular dehydrogenation (step 10) is reversed at the assumed reactor conditions, and CHO* combines with CH_3O^* to form CH_2O^*. Furthermore, given the facile desorption of CH_2O^*, this step is also irreversible. Hence, through bimolecular dehydrogenation of CHO* and CH_3O^* to CH_2O^*, the flux of further dehydrogenation of CHO* to CO*, as compared to CH_2O^* to CHO*, is reduced by a factor of 60, increasing selectivity to CH_2O. CHO* dehydrogenation to CO* possesses a low rate of due to a high barrier of 2.11 eV.

The ratio of the rate of dissociative adsorption of methanol to CH_3O^* to the rate of dissociative adsorption to form CH_2OH^* is $5x10^8$, strongly supporting the earlier conclusion from the free energy diagram, shown in Figure 6, that the CH_2OH^* pathway cannot compete with the CH_3O pathway. Further, as predicted from the free energy diagram, dehydrogenation of CH_2OH^* to CH_2O^* through the crossover pathway is quasi-equilibrated.

OH*'s (hydrogen atoms adsorbed on lattice oxygen) formed from dissociated C_1 species recombine to form H_2O^* through a pathway with a barrier of 0.10 eV. H_2O^* formation has a

degree of kinetic control of 0.47. Desorption of species such as CH_2O*, H_2O*, and CO* reduces the (010) surface, creating oxygen vacancies which will propagate the reaction. The surface is reoxidized through dissociative chemisorption of O_2, which has a degree of kinetic control of -0.47. Hence, surface oxidation is inhibitory towards methanol oxidation, leading to fewer vacancies being available for methanol chemisorption. It has been shown that the sum of degree of kinetic control for all steps should be equal to the number of independent pathways in the system[97,98]. The system investigated here, which has four independent pathways, is consistent with this rule, as the degree of kinetic control sums to 3.97. O* is the Most Abundant Reaction Intermediate (MARI), and the terminal oxygen vacancy has a coverage of only $1.15x10^{-8}$. Surface coverages of other species are shown in Table 6.

The above results are qualitatively similar to experimental findings of Chowdhry et al.,[32] who see little to no adsorption on the (010) facet in UHV conditions, and of Farenth et al.,[3] who argue that non-(010) surfaces are responsible for methanol oxidation to formaldehyde. We note, however, that as discussed below, use of energetics from the more accurate and costlier HSE06 functional does result in less oxygen poisoning of the surface and higher rates than are predicted with the standard BEEF-VdW functional. Further, a relatively low OH* (hydrogen atoms adsorbed on lattice oxygen) coverage of $7.41x10^{-9}$ shows that a phase transition to hydrogen molybdenum bronze is unlikely to occur in an oxidizing environment and at low conversion. This low coverage is due to a small barrier for hydroxyl recombination and highly favorably desorption free energy of H_2O*.

Analytical expressions for reaction rates and coverages are derived using the Langmuir Hinshelwood (LH) framework. On the basis of both large forward and reverse rates in comparison with the corresponding net reaction rates and their negligible degree of kinetic

control, adsorption/desorption of CH_3OH*, CH_2O*, CO*, H_2O* and O_2*, together with the crossover pathway (step 9), are assumed to be in quasi-equilibrium. The Pseudo-Steady State Hypothesis (PSSH) is applied to CH_3O*, CHO*, CH_2OH*, OH*, and O* intermediates. As the CH_2O* pathway is found to be significantly faster than independent pathways involving CO*, CH_2OH*, and bimolecular dehydrogenation, the kinetic expressions can be further simplified. The vacant site coverage is also approximated by assigning O* as the Most Abundant Reactive Intermediate (MARI). Detailed derivation of coverages and independent rates is provided in the Supporting Information. A comparison between the full microkinetic model and the LH model is shown in Table 6. Coverages of surface species, independent rates, degree of kinetic control for elementary steps, and apparent activation energies and orders calculated using the LH model are very close to the steady state numerical solution. Interestingly, the apparent activation energy can be directly evaluated from the free energy landscapes shown in Figure 6 and Figure 7. It consists of the sum of energy differences weighted by the corresponding degree of rate control (equation 6) between:

1. The transition state for CH_2O* formation from CH_3O* and CH_3OH in the gas phase,
2. The reaction barrier for step 11 (OH* recombination to form H_2O*), and
3. The transition state for dissociative adsorption of O_2 (vacancy oxidation step) and gas phase O_2.

Thus, although a common assumption is that the apparent activation energy is close to the highest barrier on a free energy diagram, in this case, it is actually a linear combination of barriers weighted by their respective degrees of kinetic control. The truncated rate expressions can suggest strategies for engineering higher catalytic activity for methanol oxidation through geometric and electronic modifications of the (010) surface. As the activation barrier for step 11

is quite low, the best way to improve reactivity is by reducing the binding energy of O_2, increasing the barrier for MoO_3 oxidation (k_{14}), and reducing the energy of the transition state cleaving the C – H bond of CH_3O* with respect to gas phase methanol. Such improvements might be made, for example, by substitutional doping of the oxide or by changing the geometry of the oxide facet.

$$r_1 = \frac{k_3 K_1 K_2 P'_{CH_3OH} \sqrt{k_{11}}}{\sqrt{2k_{14} K_{13} P'_{O_2}}} \tag{2}$$

$$r_5 = \frac{k_5 P'_{CH_2O} \sqrt{P'_{CH_3OH}}}{K_4 P'^{0.75}_{O_2}} \sqrt{\frac{k_3 K_1 K_2 \sqrt{k_{11}}}{(2k_{14} K_{13})^{1.5}}} \tag{3}$$

$$r_8 = k_8 P'^{1.5}_{CH_3OH} P'^{-0.75}_{O_2} \sqrt{\frac{k_3 K_1^3 K_2 \sqrt{k_{11}}}{(2k_{14} K_{13})^{1.5}}} \tag{4}$$

$$-r_{-10} = \frac{\frac{k_{-10} k_5 P'_{CH_2O}}{K_4} \sqrt{\frac{K_1^3 K_2^3 P'^3_{CH_3OH} k_3 k_{11}^{1.5}}{\left(2k_{14} K_{13} P'_{O_2}\right)^{2.5}}}}{k_6 + k_{-10} K_1 K_2 P'_{CH_3OH} \sqrt{\frac{k_{11}}{2k_{14} K_{13} P'_{O_2}}}} \approx \frac{k_5 P'_{CH_2O}}{K_4} \sqrt{\frac{K_1 K_2 k_3 P'_{CH_3OH} \sqrt{k_{11}}}{\left(2k_{14} K_{13} P'_{O_2}\right)^{1.5}}} \tag{5}$$

$$E_{apparent} = 1 * \left(G^{\ddagger}_{CH_3O*-O*} - G_{O*} - G_{CH_3OH(g)}\right) + 0.5 * \left(G^{\ddagger}_{2OH*} - 2 * G_{O*}\right) - 0.5 * \left(G^{\ddagger}_{O_2*-*} - G_{O_2(g)}\right) \tag{6}$$

To evaluate the sensitivity of our microkinetic conclusions to the choice of DFT method, we perform a similar kinetic analysis using the HSE06 free energy surface; the hybrid nature of the HSE functional should, in principle, give somewhat more accurate energetics than can be predicted from a pure GGA functional such as BEEF. From Figure 9, both BEEF-vdW and HSE06 show similar surface thermodynamics, and so the more favorable CH_3O* pathway that

leads to desorption of CH_2O*, as seen with kinetics on the BEEF-vdW free energy surface, is likely to occur with HSE06, as well. Hence, for the HSE06 analysis, the full mechanism is truncated to CH_2O formation and the redox steps of MoO_3. BEEF-vdW activation energy barriers are used, as activation barriers are relatively insensitive to functional choice and as determination of transition states with hybrid HSE06 calculations is prohibitively expensive. The rate constants are shown in the Supporting Information. The turnover frequency calculated with HSE06 is 0.34 s^{-1}, which is considerably higher than that calculated using the BEEF-vdW energetics. Consequently, the apparent activation energy is calculated to be 1.53 eV, which is 0.38 eV lower than the apparent barrier with BEEF-vdW. This difference is almost entirely due to the less favorable adsorption of O_2 (0.35 eV, on a per oxygen basis) on a vacancy with HSE06 as compared with BEEF-vdW, leading to a larger coverage of vacancies with HSE06 (4.20×10^{-4} in oxidizing conditions) and to less oxygen poisoning of the surface.

Despite differences in rates and apparent activation energies, the apparent orders and degrees of kinetic control are identical between the two functionals, showing that the mechanism remains unchanged with the more accurate HSE06 energetics. Coverages and rates from the analytical LH model developed earlier also compare favorably with the microkinetic model and are shown in the Supporting Information. Hence, although hybrid energetics are needed to accurately predict absolute rates and barriers, the mechanistic conclusions appear to be relatively insensitive to the particular electronic structure method.

As mentioned briefly earlier, instead of the catalysis proceeding through CH_3OH chemisorption on a terminal oxygen vacancy, O – H scission of physisorbed methanol on the clean (010) surface could, in principle, initiate reactivity[61]. The reactivity of the clean (010) surface is compared with that of activity on oxygen vacancies using microkinetic modeling. The

free energy diagram calculated using HSE06 for methanol oxidation on the clean surface is shown in the Supporting Information. The resulting turnover frequency for methanol oxidation on the terminal oxygen vacancies (0.34 s^{-1}) is significantly higher than that on the clean surface ($1.29x10^{-6}$). Additional details are provided in the Supporting Information.

To further evaluate the robustness of our DFT/microkinetic analysis, we compare the results with available experimental kinetic studies of methanol oxidation on MoO_3. General mechanistic conclusions from the model and experiment are in good agreement. Complete selectivity to CH_2O, as predicted by the microkinetic model, is consistent with all available experimental results[2,37,46,109–111]. In addition, the predicted predominance of the CH_3O* pathway to CH_2O is supported by multiple experimental studies[2,32,37,109,111]. Further, several measurements report C – H bond scission in CH_3O, yielding CH_2O, to be the rate determining step of the catalytic cycle[2,3,32,37,109–111]. Our DFT based microkinetic model gives the degree of rate control for CH_3O* dehydrogenation to be 0.95, again consistent with these experiments. Quantitative comparisons between model predictions and experimental results are somewhat more difficult to make, however, given the propensity of the (010) terraces to undergo substantial reconstruction after time on stream, while the present study focuses primarily on the properties of the pristine (010) terraces. Experimental measurements of activation energies are in the region of 0.87 eV – 1 eV[2,46,110,112], which are approximately one half of an eV lower than the activation energy calculated by the HSE06 functional. This difference is likely related to the restructuring of the MoO_3 basal planes, mentioned above, that occurs in concert with methanol oxidation[2,3,7,17,19]. The restructuring creates undercoordinated features on crystal shear planes, which may exhibit lower reaction barriers than the smooth features of the unreconstructed terraces.

To further evaluate the robustness of the DFT/microkinetic analysis, typical DFT errors (between ± 0.05 eV and ± 0.25 eV) in barriers of kinetically relevant elementary steps (steps 3, 11, and 14) are propagated through the microkinetic analysis, with perturbations of different magnitudes applied both in isolation and in concert to these steps.. While the rate is somewhat sensitive to these errors, with most perturbations yielding approximately order of magnitude changes in the turnover frequency, the degrees of rate control and reaction orders are largely invariant, confirming that the overall reaction mechanism and kinetic properties are insensitive to these changes (further information is provided in the Supporting Information).

To summarize the microkinetic results, the analysis has revealed that methanol oxidation proceeds through the CH_3O pathway and terminates with the desorption of CH_2O. The reaction orders with respect to CH_3OH and O_2 are 1.01 and -0.48 respectively. The CH_2O formation pathway consists of three kinetically relevant elementary steps, with degrees of kinetic control reported in parenthesis, including CH_3O* dehydrogenation (0.95), H_2O* formation (0.47), and healing oxygen vacancies through dissociation of adsorbed oxygen (-0.47). An analytical rate expression, following a Langmuir Hinshelwood approach, is formulated from these insights. Mechanistic details (reaction orders, degree of kinetic control) with the BEEF-vdW and HSE06 are similar although differences in oxygen adsorption between the two functionals are manifested in differing apparent activation energies. The high selectivity towards CH_2O, and rate determining steps determined from the degree of rate control analysis, are consistent with available experimental results[2,3,32,37,46,109–111]. In addition, a sensitivity analysis shows negligible variation in the degree of kinetic control upon propagating typical DFT errors through the microkinetic model.

Effect of Oxygen Pressure on Methanol Oxidation Catalysis

The oxygen partial pressure has a strong influence on catalysis occurring on reducible oxides such as MoO_3 because it can change the coverage of oxygen vacancies that are, in turn, binding sites for reactive intermediates. Surface science studies have shown that the morphology of the (010) surface of MoO_3 is transformed in reducing environments and under differing reaction conditions, and the (010) surface forms pits in the presence of forming gas[20]. Upon exposing the pitted surfaces to a CH_3OH/N_2 mixture, additional oxygen deficiencies are created which are accommodated through the formation of surface reliefs, as is discussed in the introduction. Moreover, the (010) surface can intercalate hydrogen to form a hydrogen molybdenum bronze in the presence of CH_3OH/N_2[16,19]. To provide more insight into these processes, we use our microkinetic model to investigate the relationship between the oxygen partial pressure, the surface state, and the turnover frequency of the catalytic cycle. The oxygen pressure range is extended from near atmospheric (prevalent in industrial reactor conditions) to UHV (typical pressures of surface science experiments). Kinetics are evaluated using the HSE06 free energy surface applied to the truncated mechanism at 623 K and for oxygen pressures ranging from 19000 Pa to $5x10^{-8}$ Pa (flow rate varying from 37.8 ml min^{-1} to 10^{-10} ml min^{-1}); BEEF-vdW and HSE06 calculations display qualitatively similar trends (see also the Supporting Information). The methanol flow rate is fixed at 20 ml min^{-1}, and changes in oxygen flow rate are balanced with that of N_2 such that the total flow rate is maintained at 200 ml min^{-1}. Conversion with respect to oxygen is 2.6% at all pressures.

Figure 11 shows the change in turnover frequency for formaldehyde formation with oxygen pressure (the figure includes the analytical expression shown in equation 2 - modified to include both O* and * in the denominator, as the MARI shifts from O* to * - for the microkinetic rate). A volcano-like dependency is observed, with the rate increasing with oxygen pressure up to ~1

Pa after which it monotonically decreases. Surface coverages of key species (CH_3OH*, CH_3O*, OH*, O* and *) as a function of oxygen pressure are shown in Figure 12. CH_3O* and OH* coverages pass through a maximum in the same region as the maximum in the rate, and the MARI shifts from O* in the high pressure region to * in the low pressure zone. The volcano-like dependency can be interpreted as a competition between too few vacancies limiting catalysis at high oxygen pressures and low O* coverage available for dehydrogenation of C_1 intermediates at low oxygen pressures. We note that the trend in reaction rates at very low oxygen pressures is qualitative in nature, since with high coverages of oxygen vacancies, crystallographic shear plane formation can cause large scale reconstructions of the (010) surface that are not directly accounted for in the microkinetic model. We additionally observe that the coverage of OH*, which is key to initiate the phase transformation to a hydrogen molybdenum bronze, never exceeds ~10^{-6}. As mentioned earlier, this is because of the facile barrier for OH* recombination and the highly exothermic H_2O desorption. At low oxygen pressures, however, the reconstructed oxide mentioned above might aid in formation of a hydrogen molybdenum bronze by providing sites which adsorb H_2O* strongly, leading to more competitive H* diffusion in comparison with H_2O* desorption[16,19].

The degree of kinetic control for key elementary steps (3, 11 and 14) as a function of oxygen pressure is shown in Figure 13. Expressions for the degree of kinetic control of these steps are shown in equations 8 to 11. One striking feature is that the volcano peak (Figure 11) is located at an oxygen partial pressure where surface oxidation has a degree of kinetic control close to 0. Thus, at the maximum, oxidation of vacancies neither inhibits nor promotes the reaction. In addition, the degrees of rate control of the other kinetically significant steps have intermediate values near the maximum, consistent with the general principle that volcano maxima often

involve a competition between multiple rate-limiting steps[113]. With decreasing oxygen pressure, the degree of kinetic control for CH_3O* dehydrogenation and H_2O* formation monotonically decreases from 1.01 and 0.48, respectively, to 0, while that of surface oxidation through gas phase oxygen increases from -0.49 to 0.92. Additional insights into this competition can be obtained by analytically evaluating the location of the volcano maximum (see Supporting Information for a derivation). As seen from equation 7, the rate expression at the volcano peak is independent of k_{14}, the rate constant of surface oxidation, K_{13}, the equilibrium constant for O_2 chemisorption, and the partial pressure of oxygen, confirming the observation that at the pressure corresponding to the maximum rate, surface oxidation should neither promote nor inhibit the methanol oxidation catalytic pathway. In contrast, the maximum rate depends sensitively on both k_3 and k_{11}, confirming the kinetic relevance of both of these steps. As the mechanism changes with decreasing oxygen pressure, the apparent activation energy (equation 12) decreases from 1.63 eV to 0.84 eV, as is shown in Figure 14. The switching between two kinetic regimes leads to a compensation[114] between the apparent activation energy and the apparent prefactor, as shown in the Constable – Cremer plot in Figure 15. In essence, a reduction in the apparent activation energy, which increases the rate, is somewhat compensated for by a reduction in the apparent prefactor near the top of the volcano. This phenomenon arises as a result of the competition between methanol oxidation and redox processes involving lattice oxygen and could be expected for flat topped volcanos such as the one shown in Figure 11.

$$r_1^{max} = k_3^{0.67} k_{11}^{0.33} \left(\frac{4}{27} K_1 K_2 P'_{CH3OH}\right)^{0.67} \quad (7)$$

$$DKC_3 = \frac{\frac{\theta_O}{\theta_*}}{1+\frac{\theta_O}{\theta_*}} \quad (8)$$

$$DKC_{11} = \frac{\frac{1\theta_O}{2\,\theta_*}}{1+\frac{\theta_O}{\theta_*}}$$

(9)

$$DKC_{14} = 1 - \frac{\frac{3\theta_O}{2\,\theta_*}}{1+\frac{\theta_O}{\theta_*}}$$

(10)

$$\frac{\theta_O}{\theta_*} = \sqrt{\frac{\left(2K_{13}k_{14}P\prime_{O_2}\right)^{1.5}}{k_3K_1K_2\sqrt{k_{11}}P\prime_{CH_3OH}}}$$

(11)

$$E_{apparent} = 1.63 - \frac{0.84}{1+2534\sqrt{\frac{P\prime_{O_2}^{1.5}}{P\prime_{CH_3OH}}}}$$

(12)

Conclusions

A detailed first principles kinetic model for methanol oxidation on the (010) terraces of MoO_3 is constructed to gain atomic-level insights into reaction pathways on this highly reducible oxide surface. The DFT-based microkinetic analysis shows that methanol oxidation proceeds through dissociative adsorption of methanol, forming CH_3O*, with methanol dissociation to CH_2OH* being kinetically and thermodynamically unfavorable. Dehydrogenation of CH_3O* to CH_2O* has a degree of kinetic control of 0.95. Further C – H scission cannot compete with facile desorption of CH_2O*, yielding complete selectivity to formaldehyde.

Moreover, dehydrogenation pathways are dominated by monomolecular hydrogenation of C_1 species with bimolecular pathways being kinetically insignificant. The most favorable route for surface hydroxyls is to form H_2O* in a pathway having a degree of rate control of 0.47. Subsequently, exothermic desorption of H_2O* leads to oxygen vacancy formation. Additionally, the exergonic desorption of H_2O* leads to low OH* coverage, preventing hydrogen intercalation under oxidizing conditions. Oxidation of the reduced surfaces proceeds through dissociative chemisorption of oxygen at a terminal oxygen defect which is rate inhibitory, having a degree of kinetic control of -0.47. Thus, the overall pathway to formaldehyde has three kinetically significant steps: C – H cleavage of CH_3O*, recombination of OH* to form H_2O*, and oxidation of the reduced surface through gas phase oxygen.

Reaction orders with respect to gas phase methanol and oxygen are 1.01 and -0.48, respectively. Microkinetic simulations with the BEEF-vdW and HSE06 functionals yield identical apparent orders and degrees of kinetic control, but apparent activation energies are 1.92 eV and 1.53 eV, respectively. This difference arises from stronger adsorption of oxygen with BEEF-vdW in comparison with HSE06. Interestingly, the apparent activation energy for formaldehyde formation is the sum of activation energies of elementary steps weighted by their degree of kinetic control.

The oxygen partial pressure not only determines the state of the surface but also strongly influences the reaction kinetics in reducible oxide catalysis. The interdependence of methanol oxidation and redox processes involving lattice oxygen is investigated by evaluating methanol oxidation kinetics across a range of oxygen partial pressures (from typical reactor inlet conditions to UHV). The turnover frequency shows a volcano like dependency with oxygen pressure, with the rate determining steps shifting from a combination of CH_3O*

dehydrogenation, H_2O* formation, and surface oxidation (degree of kinetic control of -0.49) to solely surface oxidation (degree of kinetic control of 0.92) as the oxygen partial pressure is reduced. Oxidation of surface vacancies neither inhibits nor promotes the reaction rate at the volcano maximum.

A simplified analytical form of the rate expression for the kinetics, which is valid for a wide range of oxygen pressures, is proposed in this contribution. The kinetic and thermodynamic constants in this expression might be tuned through geometric (strain, coordination environment) and electronic modifications (substitutional doping) of the (010) surface of MoO_3, suggesting strategies to enhance catalytic activity of the basal planes of MoO_3. The DFT and microkinetic modeling approach demonstrated here is generally suitable for analysis of catalytic mechanisms on reducible oxide surfaces.

Supporting Information

Electronic structure calculation and microkinetic modeling details, adsorption configurations and their energies, activation barriers of elementary steps and transition state geometries, methanol oxidation pathways on the clean (010) surface, and detailed derivation of the analytical Langmuir Hinshelwood kinetic model is presented in the Supporting Information.

Acknowledgements

Support for this research was provided National Science Foundation's program for Designing Materials to Revolutionize and Engineer our Future, DMREF (CBET-1437219). T.C. also acknowledges an Eastman Graduate Fellowship. Use of the Center for Nanoscale Materials, a U.S. Department of Energy, Office of Science, Office of Basic Energy Sciences User Facility under Contract No. DE-AC02-06CH11357, and of computational resources from the National Energy Research Scientific Computing Center, are gratefully acknowledged.

References

(1) Soares, A. P. V.; Portela, M. F.; Kiennemann, A. *Catal. Rev.* **2005**, *47*, 125–174.

(2) Farneth, W. E.; Ohuchi, F.; Staley, R. H.; Chowdhry, U.; Sleight, A. W. *J. Phys. Chem.* **1985**, *89*, 2493–2497.

(3) Farneth, W. E.; Staley, R. H.; Sleight, A. W. *J. Am. Chem. Soc.* **1986**, *108*, 2327–2332.

(4) Vohs, J. M. *Chem. Rev.* **2013**, *113*, 4136–4163.

(5) Barteau, M. A. *Chem. Rev.* **1996**, *96*, 1413–1430.

(6) Vohs, J. M.; Barteau, M. A. *Surf. Sci.* **1989**, *221*, 590–608.

(7) Chung, J. S.; Miranda, R.; Bennett, C. O. *J. Catal.* **1988**, *114*, 398–410.

(8) Keulks, G. W.; Rosynek, M. P.; Daniel, C. *Ind. Eng. Chem. Prod. Res. Dev.* **1971**, *10*, 138–142.

(9) Getsoian, A.; Shapovalov, V.; Bell, A. T. *J. Phys. Chem. C* **2013**, *117*, 7123–7137.

(10) Getsoian, A.; Bell, A. T. *J. Phys. Chem. C* **2013**, *117*, 25562–25578.

(11) Zhai, Z.; Getsoian, A.; Bell, A. T. *J. Catal.* **2013**, *308*, 25–36.

(12) Bettahar, M. M.; Costentin, G.; Savary, L.; Lavalley, J. C. *Appl. Catal. A Gen.* **1996**, *145*, 1–48.

(13) Brückman, K.; Haber, J.; Wiltowski, T. *J. Catal.* **1987**, *106*, 188–201.

(14) Mars, P.; van Krevelen, D. W. *Chem. Eng. Sci. Suppl.* **1954**, *3*, 41–59.

(15) Ressler, T.; Wienold, J.; Jentoft, R. E.; Girgsdies, F. *Eur. J. Inorg. Chem.* **2003**, *2003*, 301–312.

(16) Smith, R. L.; Rohrer, G. S. *J. Catal.* **1998**, *173*, 219–228.

(17) Smith, R. L.; Rohrer, G. S. *J. Catal.* **1998**, *180*, 270–278.

(18) Smith, R. L.; Rohrer, G. S. *J. Solid State Chem.* **1996**, *124*, 104–115.

(19) Smith, R. L.; Rohrer, G. S. *J. Catal.* **1999**, *184*, 49–58.

(20) Smith, R. L.; Rohrer, G. S. *J. Catal.* **1996**, *163*, 12–17.

(21) Barteau, M. A.; Vohs, J. M. In *Successful Design of Catalysts Future Requirements and DevelopmentProceedings ofthe Worldwide Catalysis Seminars, July, 1988, on the Occasion of the 30th Anniversary of the Catalysis Society of Japan*; Inui, T., Ed.; Studies in Surface Science and Catalysis; Elsevier, 1989; Vol. 44, pp 89–95.

(22) Farneth, W. E.; McCarron, E. M.; Sleight, A. W.; Staley, R. H. *Langmuir* **1987**, *3*, 217–223.

(23) Tatibouët, J. M.; Germain, J. E.; Volta, J. C. *J. Catal.* **1983**, *82*, 240–244.

(24) Tatibouët, J. M.; Germain, J. E. *J. Catal.* **1981**, *72*, 375–378.

(25) Al-Kandari, H.; Al-Kandari, S.; Al-Kharafi, F.; Katrib, A. *Energy Fuels* **2009**, *23*, 5737–5742.

(26) Al-Kandari, H.; Al-Kharafi, F.; Katrib, A. *J. Mol. Catal. A Chem.* **2008**, *287*, 128–134.

(27) Li, D.; Sato, T.; Imamura, M.; Shimada, H.; Nishijima, A. *Appl. Catal. B Environ.* **1998**, *16*, 255–260.

(28) Mei, D.; Karim, A. M.; Wang, Y. *J. Phys. Chem. C* **2011**, *115*, 8155–8164.

(29) Prasomsri, T.; Nimmanwudipong, T.; Roman-Leshkov, Y. *Energy Environ. Sci.* **2013**, *6*,

1732–1738.

(30) Prasomsri, T.; Shetty, M.; Murugappan, K.; Roman-Leshkov, Y. *Energy Environ. Sci.* **2014**, *7*, 2660–2669.

(31) Shetty, M.; Murugappan, K.; Prasomsri, T.; Green, W. H.; Román-Leshkov, Y. *J. Catal.* **2015**, *331*, 86–97.

(32) Chowdhry, U.; Ferretti, A.; Firment, L. E.; Machiels, C. J.; Ohuchi, F.; Sleight, A. W.; Staley, R. H. *Appl. Surf. Sci.* **1984**, *19*, 360–372.

(33) Papakondylis, A.; Sautet, P. *J. Phys. Chem.* **1996**, *100*, 10681–10688.

(34) Brookes, C.; Wells, P. P.; Cibin, G.; Dimitratos, N.; Jones, W.; Morgan, D. J.; Bowker, M. *ACS Catal.* **2014**, *4*, 243–250.

(35) Brookes, C.; Bowker, M.; Gibson, E. K.; Gianolio, D.; Mohammed, K. M. H.; Parry, S.; Rogers, S. M.; Silverwood, I. P.; Wells, P. P. *Catal. Sci. Technol.* **2016**, *6*, 722–730.

(36) Brookes, C.; Wells, P. P.; Dimitratos, N.; Jones, W.; Gibson, E. K.; Morgan, D. J.; Cibin, G.; Nicklin, C.; Mora-Fonz, D.; Scanlon, D. O.; Catlow, C. R. A.; Bowker, M. *J. Phys. Chem. C* **2014**, *118*, 26155–26161.

(37) Machiels, C. J.; Cheng, W. H.; Chowdhry, U.; Farneth, W. E.; Hong, F.; Carron, E. M. M.; Sleight, A. W. *Appl. Catal.* **1986**, *25*, 249–256.

(38) Rousseau, R.; Dixon, D. A.; Kay, B. D.; Dohnalek, Z. *Chem. Soc. Rev.* **2014**, *43*, 7664–7680.

(39) Fang, Z.; Li, Z.; Kelley, M. S.; Kay, B. D.; Li, S.; Hennigan, J. M.; Rousseau, R.; Dohnálek, Z.; Dixon, D. A. *J. Phys. Chem. C* **2014**, *118*, 22620–22634.

(40) Li, Z.; Fang, Z.; Kelley, M. S.; Kay, B. D.; Rousseau, R.; Dohnalek, Z.; Dixon, D. A. *J. Phys. Chem. C* **2014**, *118*, 4869–4877.

(41) Gregoriades, L. J.; Döbler, J.; Sauer, J. *J. Phys. Chem. C* **2010**, *114*, 2967–2979.

(42) Deshlahra, P.; Carr, R. T.; Chai, S.-H.; Iglesia, E. *ACS Catal.* **2015**, *5*, 666–682.

(43) Deshlahra, P.; Iglesia, E. *J. Phys. Chem. C* **2014**, *118*, 26115–26129.

(44) Sha, X.; Chen, L.; Cooper, A. C.; Pez, G. P.; Cheng, H. *J. Phys. Chem. C* **2009**, *113*, 11399–11407.

(45) Ding, H.; Lin, H.; Sadigh, B.; Zhou, F.; Ozoliņš, V.; Asta, M. *J. Phys. Chem. C* **2014**, *118*, 15565–15572.

(46) Cheng, W.-H. *J. Catal.* **1996**, *158*, 477–485.

(47) O'Brien, M. G.; Beale, A. M.; Jacques, S. D. M.; Buslaps, T.; Honkimaki, V.; Weckhuysen, B. M. *J. Phys. Chem. C* **2009**, *113*, 4890–4897.

(48) Bowker, M.; Carley, A. F.; House, M. *Catal. Letters* **2007**, *120*, 34–39.

(49) Bowker, M. *Top. Catal.* **2015**, *58*, 606–612.

(50) Routray, K.; Zhou, W.; Kiely, C. J.; Grünert, W.; Wachs, I. E. *J. Catal.* **2010**, *275*, 84–98.

(51) Chen, M.; Waghmare, U. V; Friend, C. M.; Kaxiras, E. *J. Chem. Phys.* **1998**, *109*, 6854–6860.

(52) Chen, M.; Friend, C. M.; Kaxiras, E. *J. Chem. Phys.* **2000**, *112*, 9617–9623.

(53) Chen, M.; Friend, C. M.; Kaxiras, E. *J. Am. Chem. Soc.* **2001**, *123*, 2224–2230.

(54) Coquet, R.; Willock, D. J. *Phys. Chem. Chem. Phys.* **2005**, *7*, 3819–3828.

(55) Ding, H.; Ray, K. G.; Ozolins, V.; Asta, M. *Phys. Rev. B* **2012**, *85*, 12104.

(56) Grimme, S. *J. Comput. Chem.* **2006**, *27*, 1787–1799.

(57) Klimeš, J.; Bowler, D. R.; Michaelides, A. *J. Phys. Condens. Matter* **2010**, *22*, 22201.

(58) Chen, L.; Cooper, A. C.; Pez, G. P.; Cheng, H. *J. Phys. Chem. C* **2008**, *112*, 1755–1758.

(59) Ritter, C.; Müller-Warmuth, W.; Schöllhorn, R. *J. Chem. Phys.* **1985**, *83*, 6130–6138.

(60) Huang, P. R.; He, Y.; Cao, C.; Lu, Z. H. *Sci. Rep.* **2014**, *4*, 7131.

(61) Rellán-Piñeiro, M.; López, N. *ChemSusChem* **2015**, *8*, 2231–2239.

(62) Kresse, G.; Hafner, J. *Phys. Rev. B* **1993**, *48*, 13115–13118.

(63) Kresse, G.; Furthmüller, J. *Comput. Mater. Sci.* **1996**, *6*, 15–50.

(64) Kresse, G.; Hafner, J. *Phys. Rev. B* **1994**, *49*, 14251–14269.

(65) Blöchl, P. E. *Phys. Rev. B* **1994**, *50*, 17953–17979.

(66) Kresse, G.; Joubert, D. *Phys. Rev. B* **1999**, *59*, 1758–1775.

(67) Marsman, M.; Kresse, G. *J. Chem. Phys.* **2006**, *125*, 104101.

(68) Wellendorff, J.; Lundgaard, K. T.; Møgelhøj, A.; Petzold, V.; Landis, D. D.; Nørskov, J. K.; Bligaard, T.; Jacobsen, K. W. *Phys. Rev. B* **2012**, *85*, 235149.

(69) Heyd, J.; Scuseria, G. E. *J. Chem. Phys.* **2004**, *121*, 1187–1192.

(70) Heyd, J.; Scuseria, G. E.; Ernzerhof, M. *J. Chem. Phys.* **2003**, *118*, 8207–8215.

(71) Heyd, J.; Scuseria, G. E.; Ernzerhof, M. *J. Chem. Phys.* **2006**, *124*, 219906.

(72) Monkhorst, H. J.; Pack, J. D. *Phys. Rev. B* **1976**, *13*, 5188–5192.

(73) Negishi, H.; Negishi, S.; Kuroiwa, Y.; Sato, N.; Aoyagi, S. *Phys. Rev. B* **2004**, *69*, 64111.

(74) Henkelman, G.; Arnaldsson, A.; Jónsson, H. *Comput. Mater. Sci.* **2006**, *36*, 354–360.

(75) Sanville, E.; Kenny, S. D.; Smith, R.; Henkelman, G. *J. Comput. Chem.* **2007**, *28*, 899–908.

(76) Henkelman, G.; Uberuaga, B. P.; Jónsson, H. *J. Chem. Phys.* **2000**, *113*, 9901–9904.

(77) Henkelman, G.; Jónsson, H. *J. Chem. Phys.* **2000**, *113*, 9978–9985.

(78) Henkelman, G.; Jónsson, H. *J. Chem. Phys.* **1999**, *111*, 7010–7022.

(79) Momma, K.; Izumi, F. *J. Appl. Crystallogr.* **2011**, *44*, 1272–1276.

(80) Wang, L.; Maxisch, T.; Ceder, G. *Phys. Rev. B* **2006**, *73*, 195107.

(81) Grindy, S.; Meredig, B.; Kirklin, S.; Saal, J. E.; Wolverton, C. *Phys. Rev. B* **2013**, *87*, 75150.

(82) Zeng, Z.; Calle-Vallejo, F.; Mogensen, M. B.; Rossmeisl, J. *Phys. Chem. Chem. Phys.* **2013**, *15*, 7526–7533.

(83) Zeng, Z.; Chan, M. K. Y.; Zhao, Z.; Kubal, J.; Fan, D.; Greeley, J. *J. Phys. Chem. C* **2015**, *119*, 18177–18187.

(84) Antony, A.; Asthagiri, A.; Weaver, J. F. *Phys. Chem. Chem. Phys.* **2012**, *14*, 12202–12212.

(85) Campbell, C. T.; Sellers, J. R. V. *J. Am. Chem. Soc.* **2012**, *134*, 18109–18115.

(86) Campbell, C. T.; Sellers, J. R. V. *Chem. Rev.* **2013**, *113*, 4106–4135.

(87) Campbell, C. T.; Árnadóttir, L.; Sellers, J. R. V. *Zeitschrift für Phys. Chemie* **2013**, *227*, 1–20.

(88) Hill, T. L. In *An Introduction to Statistical Thermodynamics*; Dover Publications, Inc., New York, 1986; pp 172–176.

(89) Cortright, R. D.; Dumesic, J. A. Advances in Catalysis; Academic Press, 2001; Vol. 46, pp 161–264.

(90) Singh, S.; Li, S.; Carrasquillo-Flores, R.; Alba-Rubio, A. C.; Dumesic, J. A.; Mavrikakis, M. *AIChE J.* **2014**, *60*, 1303–1319.

(91) Kandoi, S.; Greeley, J.; Sanchez-Castillo, M. A.; Evans, S. T.; Gokhale, A. A.; Dumesic, J. A.; Mavrikakis, M. *Top. Catal. 37*, 17–28.

(92) Gokhale, A. A.; Kandoi, S.; Greeley, J. P.; Mavrikakis, M.; Dumesic, J. A. *Chem. Eng. Sci.* **2004**, *59*, 4679–4691.

(93) Grabow, L. C.; Gokhale, A. A.; Evans, S. T.; Dumesic, J. A.; Mavrikakis, M. *J. Phys. Chem. C* **2008**, *112*, 4608–4617.

(94) Clay, J. P.; Greeley, J. P.; Ribeiro, F. H.; Delgass, W. N.; Schneider, W. F. *J. Catal.* **2014**, *320*, 106–117.

(95) Behtash, S.; Lu, J.; Walker, E.; Mamun, O.; Heyden, A. *J. Catal.* **2016**, *333*, 171–183.

(96) Salciccioli, M.; Stamatakis, M.; Caratzoulas, S.; Vlachos, D. G. *Chem. Eng. Sci.* **2011**, *66*, 4319–4355.

(97) Stegelmann, C.; Andreasen, A.; Campbell, C. T. *J. Am. Chem. Soc.* **2009**, *131*, 8077–8082.

(98) Wolcott, C. A.; Medford, A. J.; Studt, F.; Campbell, C. T. *J. Catal.* **2015**, *330*, 197–207.

(99) Greeley, J.; Mavrikakis, M. *J. Am. Chem. Soc.* **2004**, *126*, 3910–3919.

(100) Lausche, A. C.; Hummelshøj, J. S.; Abild-Pedersen, F.; Studt, F.; Nørskov, J. K. *J. Catal.* **2012**, *291*, 133–137.

(101) Kristoffersen, H. H.; Metiu, H. *J. Phys. Chem. C* **2015**, *119*, 10500–10506.

(102) Mei, D.; Ge, Q.; Szanyi, J.; Peden, C. H. F. *J. Phys. Chem. C* **2009**, *113*, 7779–7789.

(103) Metiu, H.; Chrétien, S.; Hu, Z.; Li, B.; Sun, X. *J. Phys. Chem. C* **2012**, *116*, 10439–10450.

(104) Schneider, W. F.; Hass, and K. C.; Miletic, M.; Gland, J. L. *J. Phys. Chem. B* **2002**, *106*, 7405–7413.

(105) Chrétien, S.; Metiu, H. *J. Phys. Chem. C* **2015**, *119*, 19876–19882.

(106) Chrétien, S.; Metiu, H. *J. Phys. Chem. C* **2014**, *118*, 27336–27342.

(107) NIST Chemistry WebBook http://webbook.nist.gov/chemistry/.

(108) Ferrin, P.; Simonetti, D.; Kandoi, S.; Kunkes, E.; Dumesic, J. A.; Nørskov, J. K.; Mavrikakis, M. *J. Am. Chem. Soc.* **2009**, *131*, 5809–5815.

(109) Machiels, C. J.; Sleight, A. W. *J. Catal.* **1982**, *76*, 238–239.

(110) Tatibouët, J. M. *Appl. Catal. A Gen.* **1997**, *148*, 213–252.

(111) Yang, T.-J.; Lunsford, J. H. *J. Catal.* **1987**, *103*, 55–64.

(112) Pernicone, N.; Lazzerin, F.; Liberti, G.; Lanzavecchia, G. *J. Catal.* **1969**, *14*, 391–393.

(113) Greeley, J.; Stephens, I. E. L.; Bondarenko, A. S.; Johansson, T. P.; Hansen, H. A.; Jaramillo, T. F.; Rossmeisl, J.; Chorkendorff, I.; Nørskov, J. K. *Nat Chem* **2009**, *1*, 552–556.

(114) Bligaard, T.; Honkala, K.; Logadottir, A.; Norskov, J. K.; Dahl, S.; Jacobsen, C. J. H. *J. Phys. Chem. B* **2003**, *107*, 9325–9331.

Tables and Figures

Table 1: Terminal oxygen vacancy formation energies (referenced to 0.5 O_2 (g)), binding energies of CH_3OH* and O_2*, and Bader charges of Mo atoms as a function of supercell size. An (Xx1xY) supercell represents X and Y octahedra along [100] and [001] directions, respectively. Entries in bold indicate geometry-optimized HSE06 calculations. All other entries are calculated with BEEF-vdW. Figure 2 shows the geometry of vacancies and locations of Mo - 1 to Mo – 4.

	Vacancy Formation Energy, eV	Bader Charges of Mo atoms around the vacancy (Figure 2)				Binding Energies, eV	
Supercell Size		Mo - 1	Mo - 2	Mo - 3	Mo - 4	CH_3OH*	O_2*
2x1x2	3.08	3.12	3.37		3.69	-0.81	-2.60
3x1x3	2.58	3.31	3.2	3.62		-0.47	-2.13
4x1x3	2.57	3.32	3.21	3.61		-0.53	-2.11
3x1x4	2.36	3.51	3.24	3.42		-0.31	-1.90
4x1x4	2.34	3.50	3.24	3.41		-0.27	-1.88
5x1x4	2.35	3.41	3.21	3.40		-0.31	-1.89
4x1x5	2.26	3.60	3.38	3.30		-0.21	-1.80
5x1x5	2.24	3.59	3.38	3.3		-0.19	-1.79
2x1x2	**2.84**	**3.6**	**3.23**		**3.91**	**-0.90**	**-1.85**
3x1x3	**2.14**	**3.54**	**3.4**	**3.94**	**3.91**	**-0.56**	**-1.28**

Table 2: Binding energies of key species (referenced to energies of corresponding gas phase radicals) involved in the methanol oxidation catalytic cycle. Bader charges of surrounding Mo atoms are reported. Calculations are performed with BEEF-vdW using the 4x1x4 unit cell. The position of Mo – 1, Mo – 2 and Mo – 3 is given in Figure 3.

		Bader Charges		
Adsorbate	Binding energy (eV)	Mo – 1	Mo - 2	Mo - 3
CH_3OH*	-0.27	3.10	3.61	3.69
CH_3O*	-2.14	3.52	3.71	3.69
H_2O*	0.05	3.08	3.65	3.71
CH_2O*	-0.48	3.04	3.73	3.71
O_2*	-1.88	3.45	3.73	3.72
CO*	-0.12	2.91	3.66	3.72
CHOH*	-2.28	2.98	3.72	3.71
CHO*	-2.35	3.10	3.41	3.27
CH_2OH*	-1.59	3.08	3.28	3.31
COH*	-1.89	3.02	3.30	3.31

Table 3: Entropies of surface and gas phase species at 623.15 K, 1 atm. Gas phase entropies are taken from the NIST Chemistry WebBook.

Gas Phase	S° (J/mol K)	Molecular adsorbates	S° (J/mol K)	Molecular fragments	S° (J/mol K)
		CS equation		Hindered translation equation	
CH_3OH	282.8	CH_3OH*	170.5	CH_3O*	140.4
CH_2O	249.3	CH_2O*	147.1	CHO*	80.5
CO	194.6	CO*	108.9	CH_2OH*	140.4
H_2O	214.4	H_2O*	122.7	COH*	80.5
O_2	227.7	Harmonic oscillator		Harmonic oscillator	
		O_2*	61.3	OH*	55.8
				O*	31.9
				CHOH*	88.4

Table 4: Diffusion barriers for species on the (010) surface. Transition state geometries are shown in Figures S9, S10 and S11 in the Supporting Information.

Diffusion pathway	Activation Energy, eV
CH_3O* - top site to top site	1.48
CH_2O* - bridge to vertical	1.00
CH_2O* - button to vertical	0.77
CH_2O* - vertical to carbonate	0.53
CHO* - bridge to bridge	1.51
CHO* - bridge to button	1.97
CHO* - button to C bound state	0.22
H* terminal O to terminal O	0.46
H* terminal O to asymmetric O	0.57
H* asymmetric O to symmetric O	1.17

Table 5: Activation energies (E_a), free energy changes (ΔG), forward (k_i) and reverse (k_{-i}) rate constants for elementary steps considered in the microkinetic model. The Degree of Kinetic Control (DKC) computed through the microkinetic model is also reported.

No.	Elementary Step	E_a (eV)	ΔG (eV)	k_i (s^{-1})	k_{-i}(s^{-1})	DKC
1	$CH_3OH + * \leftrightarrow CH_3OH*$	0.00	0.46	$1.86x10^{3}$	$9.15x10^{11}$	0.00
2	$CH_3OH* + O* \leftrightarrow CH_3O* + OH*$	0.37	0.27	$1.25x10^{10}$	$2.54x10^{12}$	0.02
3	$CH_3O* + O* \leftrightarrow CH_2O* + OH*$	1.26	0.36	$8.12x10^{2}$	$6.78x10^{5}$	0.95
4	$CH_2O* \leftrightarrow CH_2O + *$	0.00	-0.18	$5.54x10^{9}$	$1.93x10^{3}$	0.00
5	$CH_2O* + O* \leftrightarrow CHO* + OH*$	1.30	-0.06	$4.22x10^{2}$	$1.51x10^{2}$	1.00
6	$CHO* + O* \leftrightarrow CO* + OH*$	2.11	0.72	$1.26x10^{-4}$	$8.50x10^{1}$	0.98
7	$CO* \leftrightarrow CO + *$	0.00	-0.44	$6.64x10^{11}$	$1.99x10^{3}$	0.00
8	$CH_3OH* + O* \leftrightarrow CH_2OH* + OH*$	1.62	0.54	$1.00x10^{0}$	$2.32x10^{4}$	1.00
9	$CH_2OH* + O* \leftrightarrow CH_2O* + OH*$	0.26	0.11	$1.03x10^{11}$	$7.58x10^{11}$	0.00
10	$2CH_2O* \leftrightarrow CH_3O* + CHO*$	0.62	-0.42	$1.21x10^{8}$	$5.18x10^{4}$	0.02
11	$2OH* \leftrightarrow H_2O* + O*$	0.10	-0.66	$2.10x10^{12}$	$1.05x10^{7}$	0.47
12	$H_2O* \leftrightarrow H_2O + *$	0.00	-0.64	$3.99x10^{13}$	$2.49x10^{3}$	0.00
13	$O_2 + * \leftrightarrow O_2*$	0.00	-0.81	$1.87x10^{3}$	$5.84x10^{1}$	0.00
14	$O_2* + * \leftrightarrow 2O*$	0.90	-2.82	$7.25x10^{5}$	$1.14x10^{-17}$	-0.47

Table 6: Steady state coverages of surface species, independent rates, apparent activation energy, and apparent reaction orders calculated with the microkinetic model and Langmuir Hinshelwood model. Reaction conditions are 10% CH_3OH, 19% O_2, balance N_2, 623.15 K 1 atm., and 5% conversion. The BEEF-vdW free energy surface is used.

Adsorbate	Microkinetic model	Langmuir Hinshelwood model
θ_{CH_3OH}	$2.25\text{x}10^{-13}$	$2.29\text{x}10^{-13}$
θ_{CH_3O}	$1.43\text{x}10^{-7}$	$1.49\text{x}10^{-7}$
θ_{CH_2O}	$1.97\text{x}10^{-12}$	$2.05\text{x}10^{-12}$
θ_{CHO}	$1.10\text{x}10^{-7}$	$1.11\text{x}10^{-7}$
θ_{CO}	$2.04\text{x}10^{-21}$	$2.14\text{x}10^{-21}$
θ_{CH_2OH}	$1.08\text{x}10^{-19}$	$1.14\text{x}10^{-19}$
θ_{H_2O}	$3.54\text{x}10^{-16}$	$3.68\text{x}10^{-16}$
θ_{OH}	$7.42\text{x}10^{-9}$	$7.54\text{x}10^{-9}$
θ_{O_2}	$6.93\text{x}10^{-3}$	$7.04\text{x}10^{-4}$
θ_O	$9.93\text{x}10^{-1}$	$9.93\text{x}10^{-1}$
θ_*	$1.15\text{x}10^{-8}$	$1.17\text{x}10^{-8}$
r_1 (s^{-1})	$1.15\text{x}10^{-4}$	$1.21\text{x}10^{-4}$
r_5 (s^{-1})	$8.29\text{x}10^{-10}$	$8.71\text{x}10^{-10}$
r_8 (s^{-1})	$2.23\text{x}10^{-13}$	$2.30\text{x}10^{-13}$
$-r_{10}$ (s^{-1})	$8.15\text{x}10^{-10}$	$8.57\text{x}10^{-10}$
Apparent activation energy (eV)	1.92	2.00
Methanol Order	1.01	1.00
Oxygen Order	-0.48	-0.50

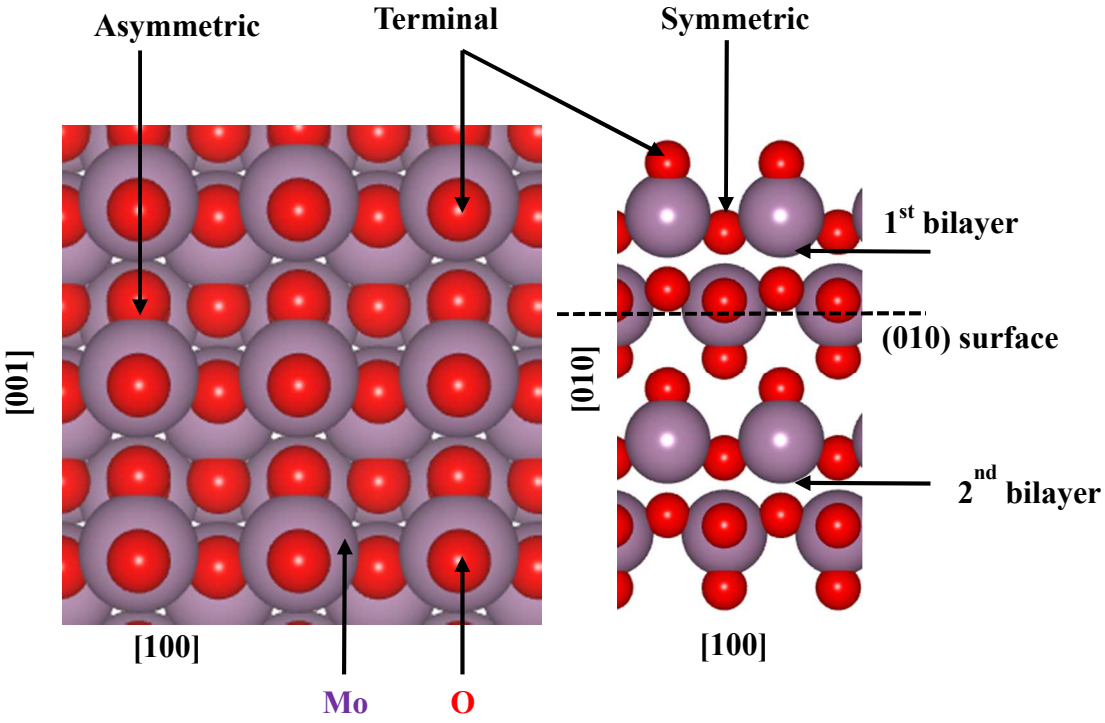

Figure 1: Top (left) and side (right) views of the (010) surface of MoO_3. The terminal, asymmetric, and symmetric oxygen atoms are shown. Mo atoms are depicted in purple while O is shown in red.

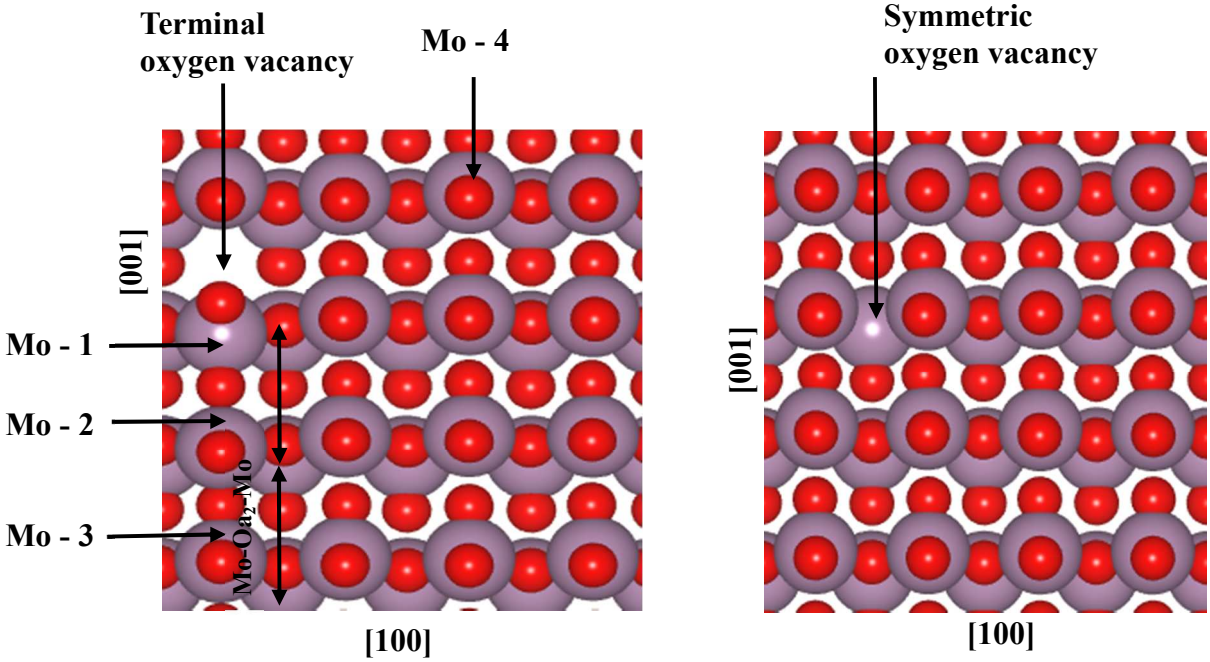

Figure 2: Terminal (left) and symmetric (right) oxygen vacancy geometries. Bader charges are calculated for the three Mo atoms near the vacancy (Mo – 1, Mo – 2 and Mo – 3) and for one Mo atom (Mo – 4) away from the vacancy. There is a noticeable compression in Mo – asymmetric oxygen bonds adjacent to the terminal defect. Mo – Oa_1 – Mo and Mo – Oa_2 – Mo bond lengths are listed in the Supporting Information. Mo atoms are shown in purple while O atoms are depicted in red.

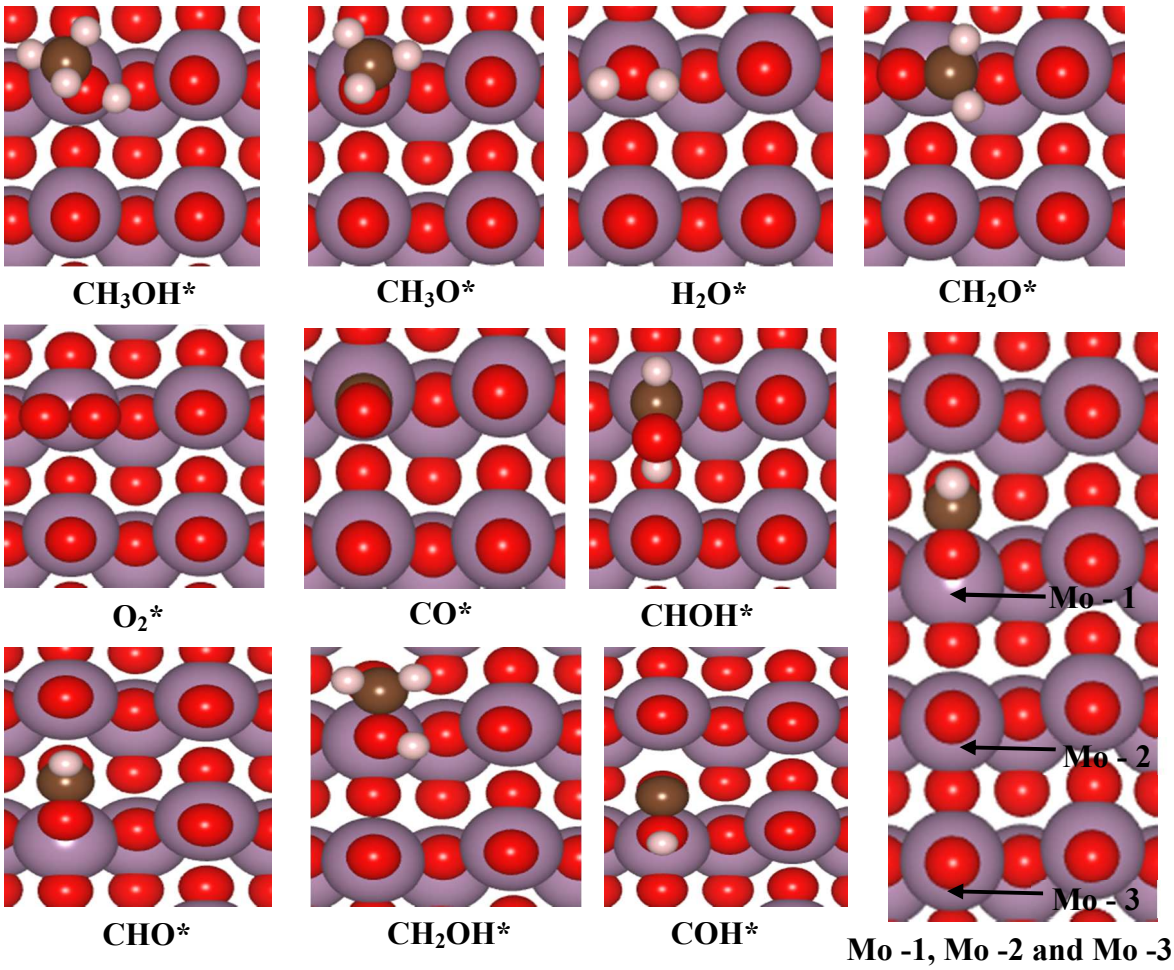

Figure 3: Top views of the most stable adsorption configurations involved in the methanol oxidation mechanism. CH_2O* and O_2* adsorb in a button configuration, while CHO*, CH_2OH* and COH* bind to the oxygen vacancy in a bridge configuration. Additional geometries are provided in Figures S1 to S6 in the Supporting Information. Mo, O, H and C are shown in purple, red, white and brown, respectively. Bader charges of Mo atoms (Mo -1, Mo -2 and Mo -3) for each adsorbate are listed in Table 2.

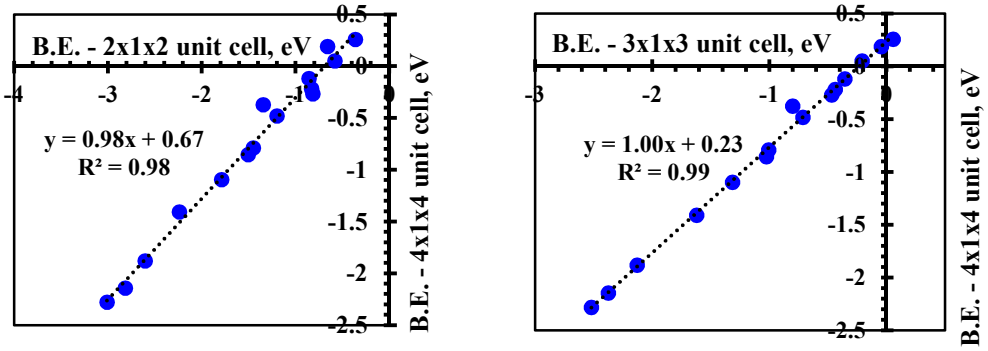

Figure 4: Binding energies on the (4x1x4) unit cell scale linearly with those calculated on the 2x1x2 (left) and 3x1x3 (right) unit cells. The intercept represents an average shift in the binding energy as the unit cell size is increased. This relationship is valid for all adsorbates that do not form a bond with the asymmetric oxygen atom. Binding energies of adsorbates that form a C – O bond with the asymmetric oxygen atom (CHO*, CH_2OH*, COH*) are invariant with unit cell size.

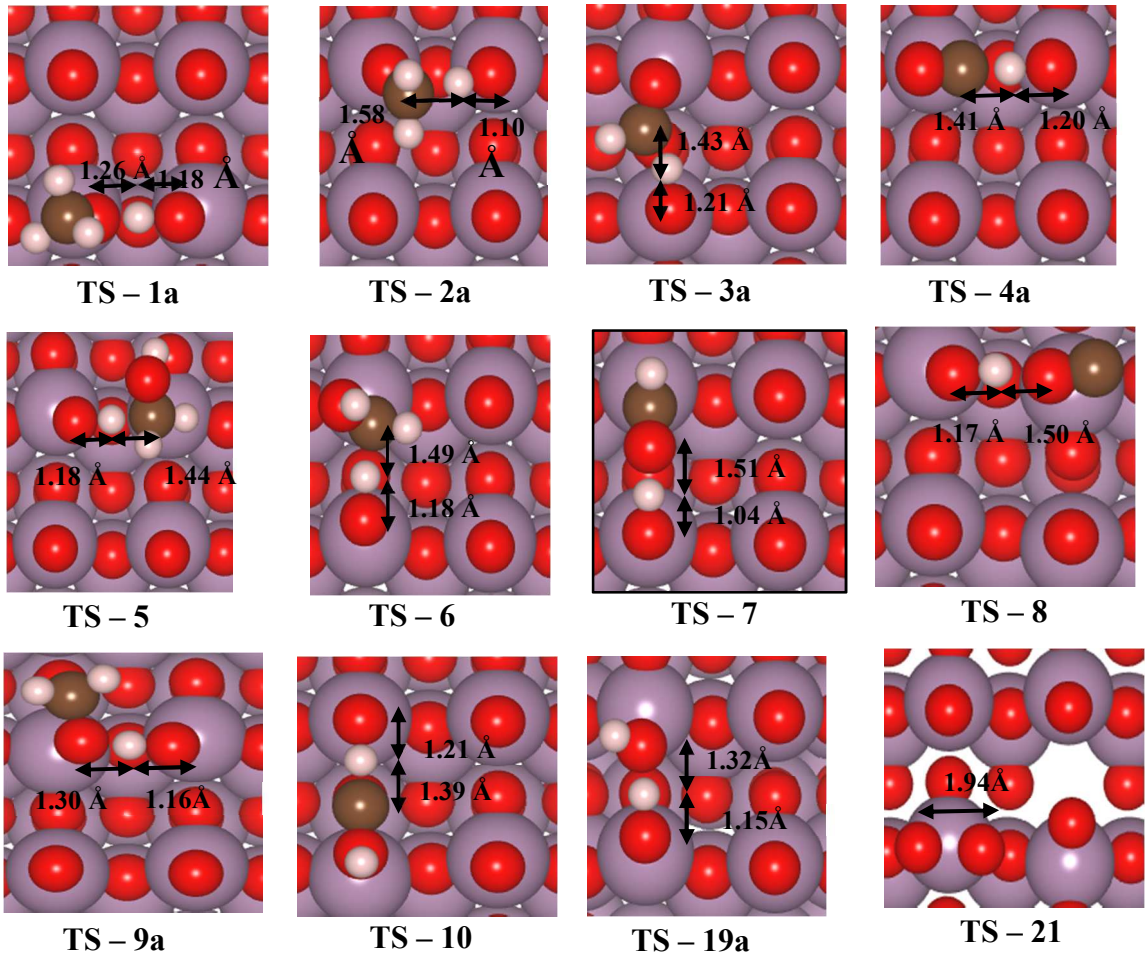

Figure 5: Geometries of transition states involved in methanol oxidation and surface redox pathways. Transition state energies are depicted in the free energy diagrams given in Figure 6 and Figure 7. These represent pathways having the lowest activation barrier. A comprehensive list of transition states is shown in Figure S7 to S12 in the Supporting Information. Mo, O, H and C atoms are shown in purple, red, white, and brown, respectively.

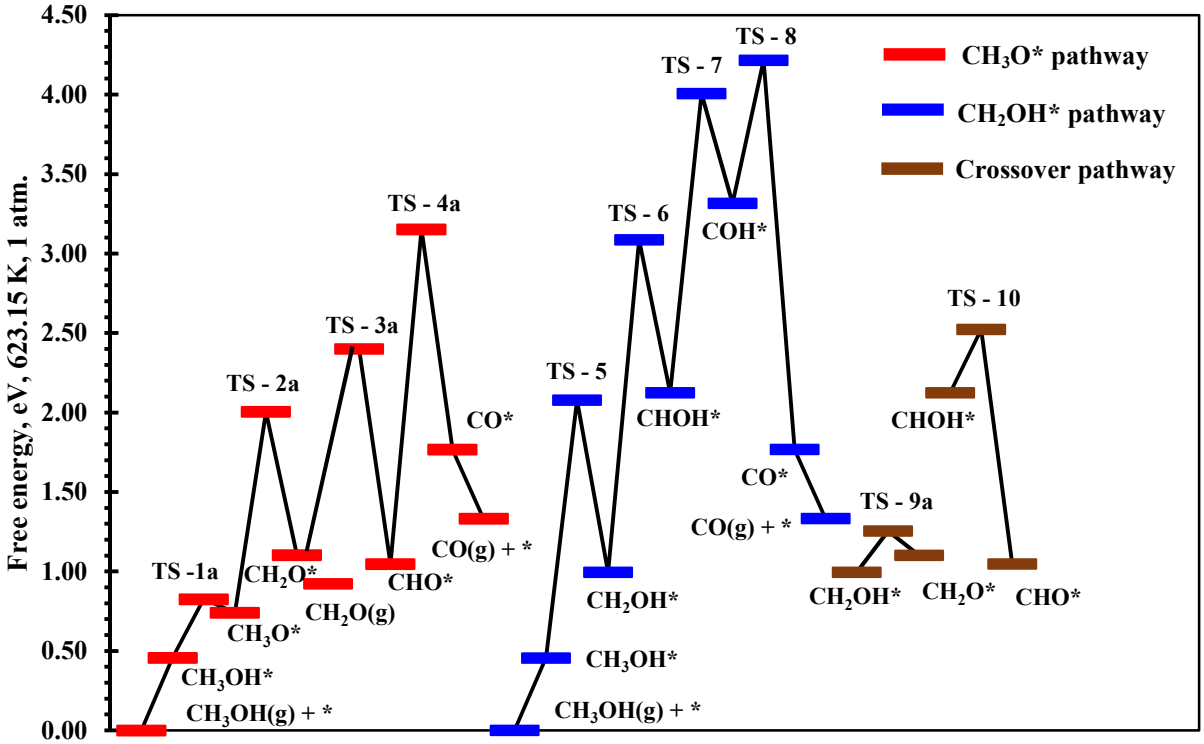

Figure 6: Free energy surface for methanol oxidation on the (010) surface of MoO_3. The CH_3O* (red), CH_2OH* (blue), and crossover (brown) pathways are shown. Free energies are referenced to CH_3OH (g) + * and evaluated at 623.15 K, 1 atm. Transition state images are provided in Figure 5.

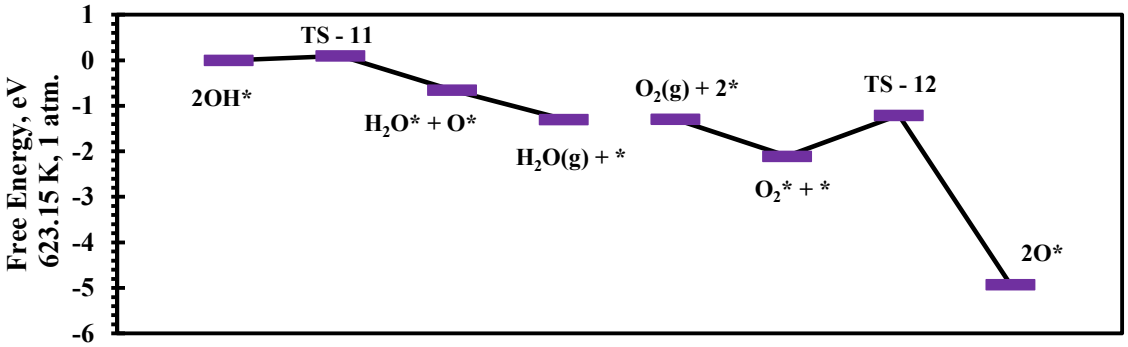

Figure 7: Free energy landscape for reduction of the (010) surface through formation of H_2O* followed by oxidation of the surface through dissociation of chemisorbed oxygen. Free energies are calculated at 623.15 K, 1 atm. and referenced to 2OH* + O_2(g) + *. It is assumed that methanol oxidation is terminated at CH_2O, thereby releasing only 2 OH*'s on the surface. Transition state images are shown in Figure 5

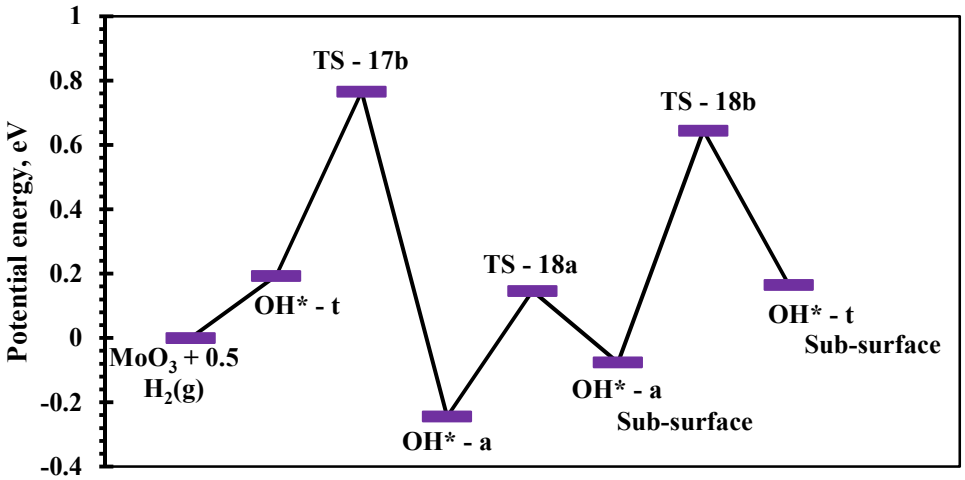

Figure 8: Hydrogen diffusion barriers within the MoO_3 lattice. The potential energy is referenced to MoO_3 + 0.5 H_2 (g). This pathway shows hydrogen movement from a surface terminal oxygen atom to a subsurface terminal oxygen in the 2nd bilayer.

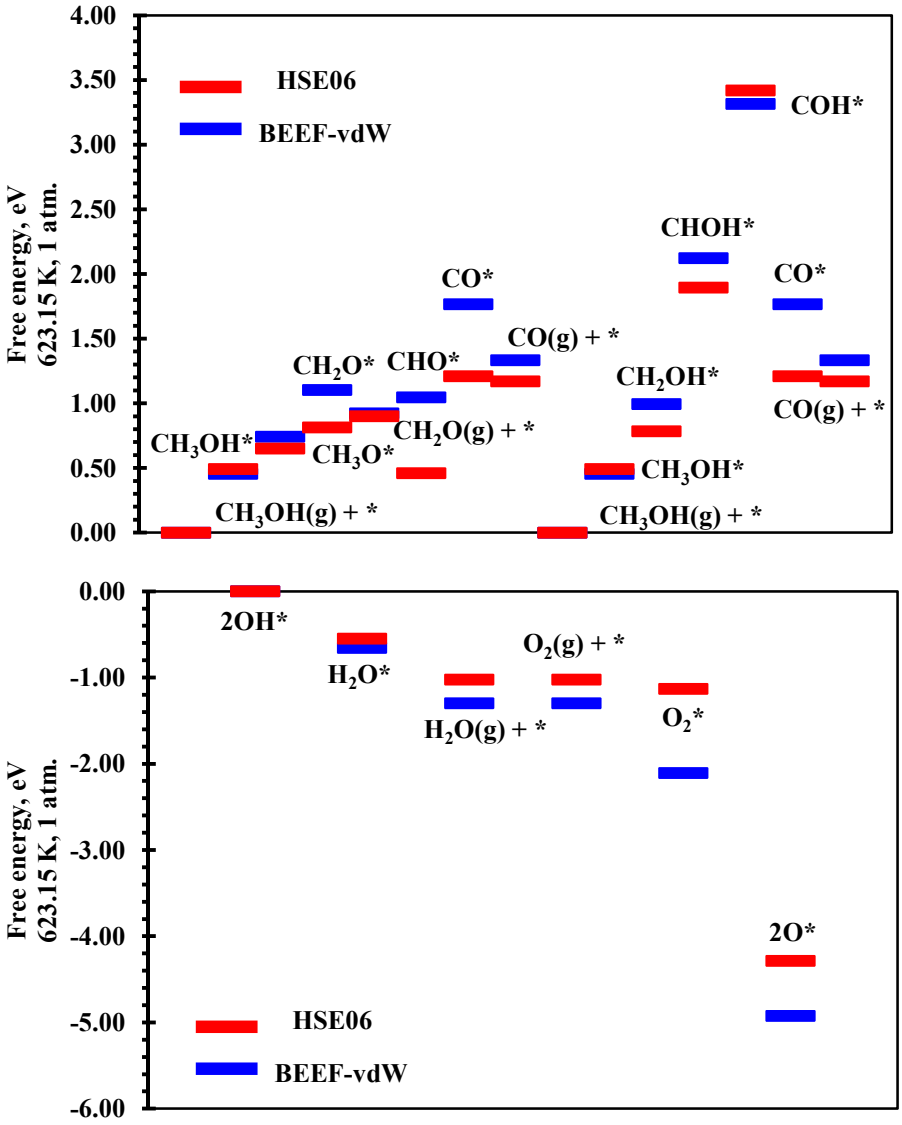

Figure 9: (Above) Comparison between methanol oxidation pathways calculated using BEEF-vdW and HSE06. Free energies for methanol oxidation pathways are referenced to CH_3OH (g) + $0.5O_2$ (g) + * and calculated at 623.15 K, 1 atm. (Below) comparison between BEEF-vdW and HSE06 computed pathways involving surface reduction and oxidation. Free energies are referenced to 2OH* + * + O_2(g). Geometry-optimized HSE06 energies are calculated on 2x1x2 unit cells. These energies are subsequently extrapolated to the 4x1x4 unit cell through the relationship shown in Figure 4. Trends in surface reaction energetics between both functionals are similar. Adsorption of oxygen, however, is more exothermic by 0.69 eV with BEEF-vdW as compared to HSE06.

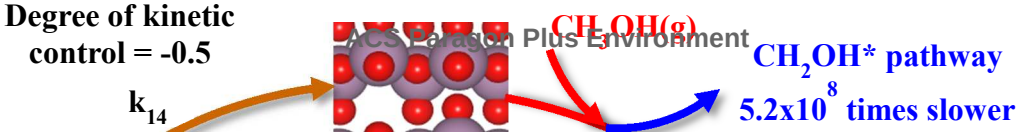

Figure 10: The catalytic cycle for methanol oxidation on MoO_3 (010) is split into two parts: methanol oxidation on terminal oxygen vacancies (red) and redox processes occurring on the surface (purple). Through stoichiometry, two methanol oxidation turnovers occur for every surface oxidation step. Methanol adsorption and ensuing O – H scission is quasi-equilibrated. C – H scission for methanol is significantly slower in comparison with O – H scission. Dehydrogenation of CH_3O* has a degree of kinetic control of 1.0. Desorption of CH_2O* is quasi-equilibrated and is significantly faster than its monomolecular or bimolecular dehydrogenation. Recombination of OH*'s forming H_2O* has a degree of rate control of 0.5. H_2O* and CH_2O* desorption regenerates vacancies which are oxidized by O_2 (degree of rate control -0.5). Mo, O, H and C are shown in purple, red, white, and brown, respectively.

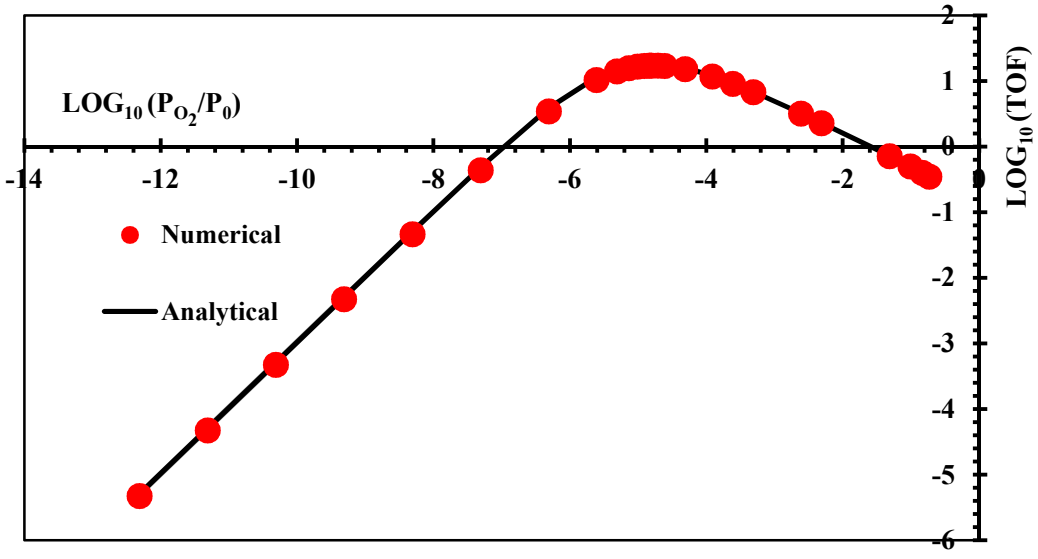

Figure 11: Effect of oxygen partial pressure on the turnover frequency of methanol oxidation on MoO_3 (010) at 623.15 K. Red dots represent the numerical solution while the black line shows the analytical LH model, equation (110) from the Supporting Information. Kinetics are computed using the HSE06 free energy surface at 623.15 K with oxygen pressure varying from typical industrial conditions (18.9 kPa) to UHV ($5x10^{-11}$ kPa).

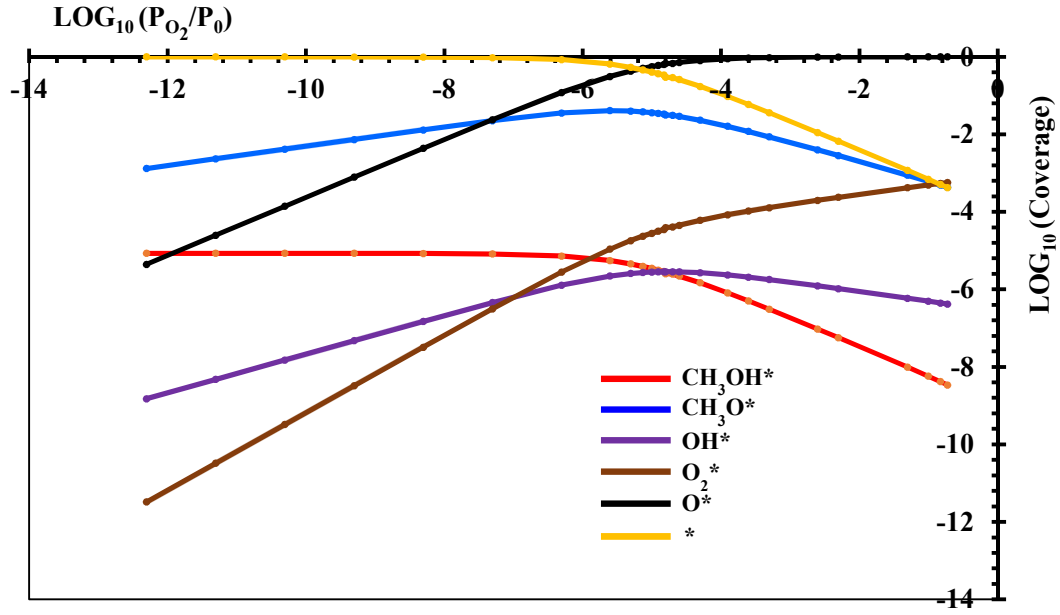

Figure 12: Surface coverages of key reactive intermediates (CH_3OH*, CH_3O*, OH*, O_2*, O* and *) as a function of oxygen partial pressure at 623.15 K.

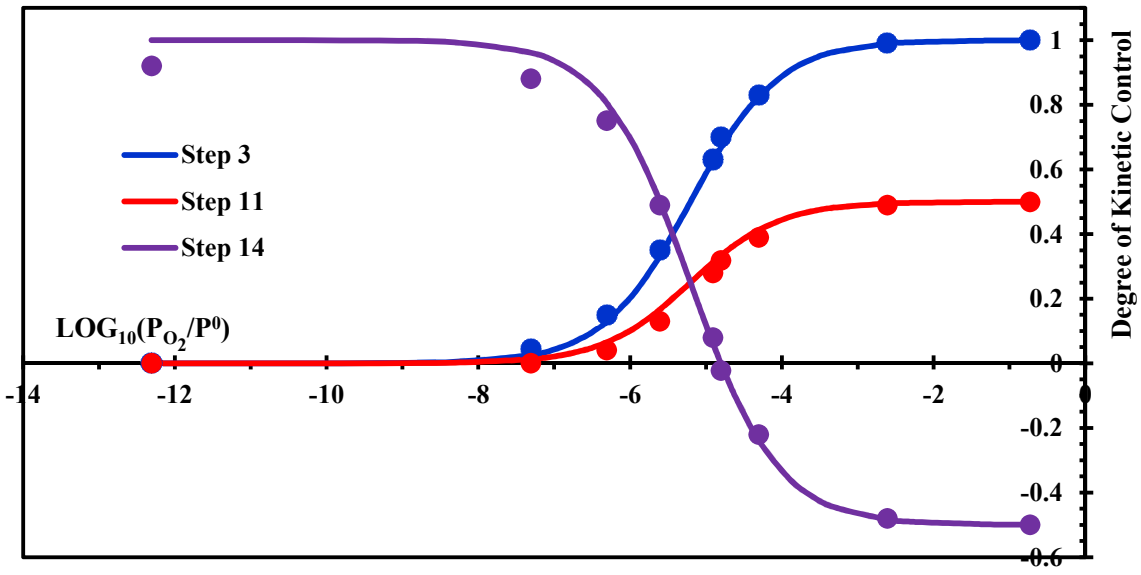

Figure 13: Degree of Kinetic Control (DKC) of CH_3O^* dehydrogenation (step 3), H_2O^* formation (step 11), and surface oxidation (step 14) as a function of the oxygen partial pressure. Circles show the numerical solution while black lines represent equations 8,9, and 10. DKC is calculated on the HSE06 free energy surface at 623.15 K.

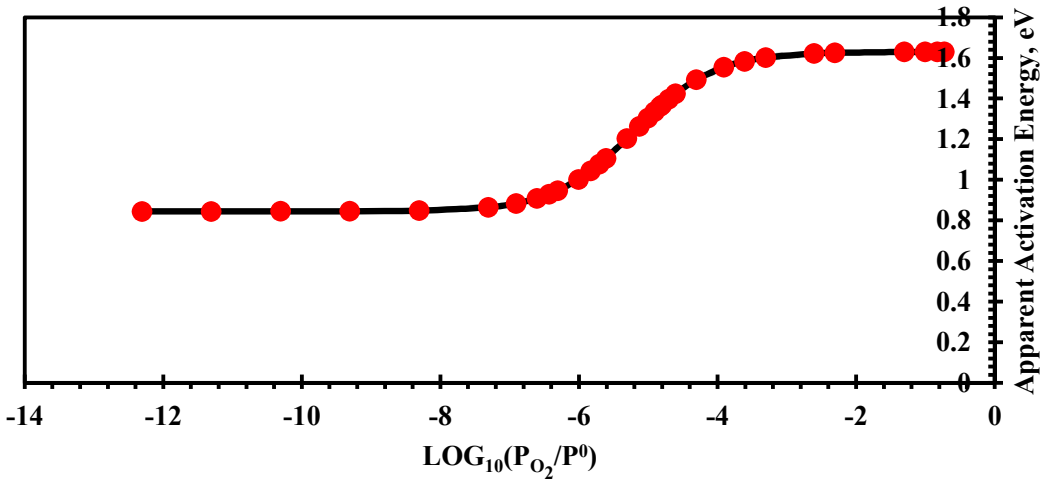

Figure 14: Apparent activation energy (computed using equation 12) as a function of the oxygen partial pressure. This is calculated with the HSE06 functional at 623.15 K. The apparent activation energy shifts from 1.63 eV to 0.84 eV as oxygen pressure varies from typical industrial conditions (18.9 kPa) to UHV ($5x10^{-11}$ kPa). This is consistent with shifts in the mechanism as seen in Figure 13

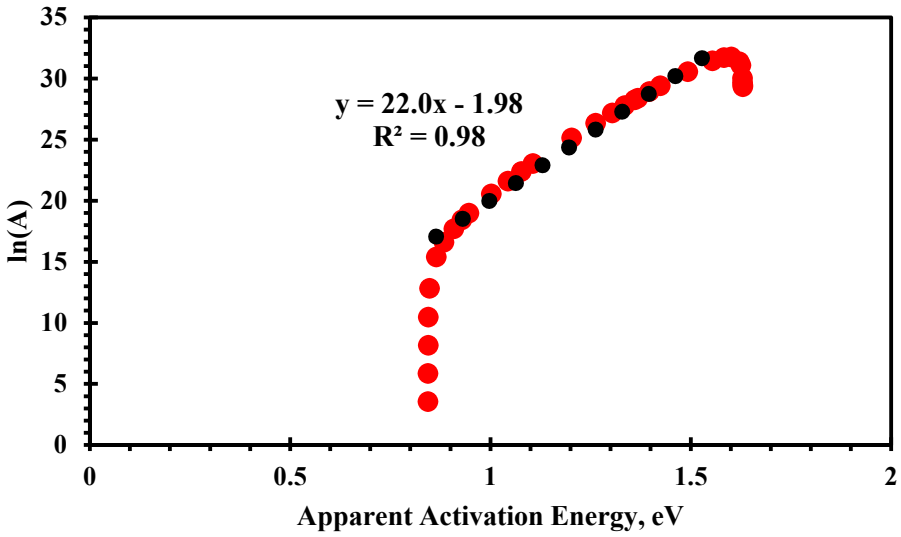

Figure 15: ln(A), the logarithm of apparent prefactor versus the apparent activation energy (constable plot). The linear range (black dotted line) shows the Constable – Cremer relationship. This effect arises as a result of a shift in the kinetics caused by variation of the partial pressure of oxygen from typical industrial conditions (18.9 kPa) to UHV ($5x10^{-11}$ kPa). Each circle corresponds to an oxygen pressure in this range.

For Table of Contents Only